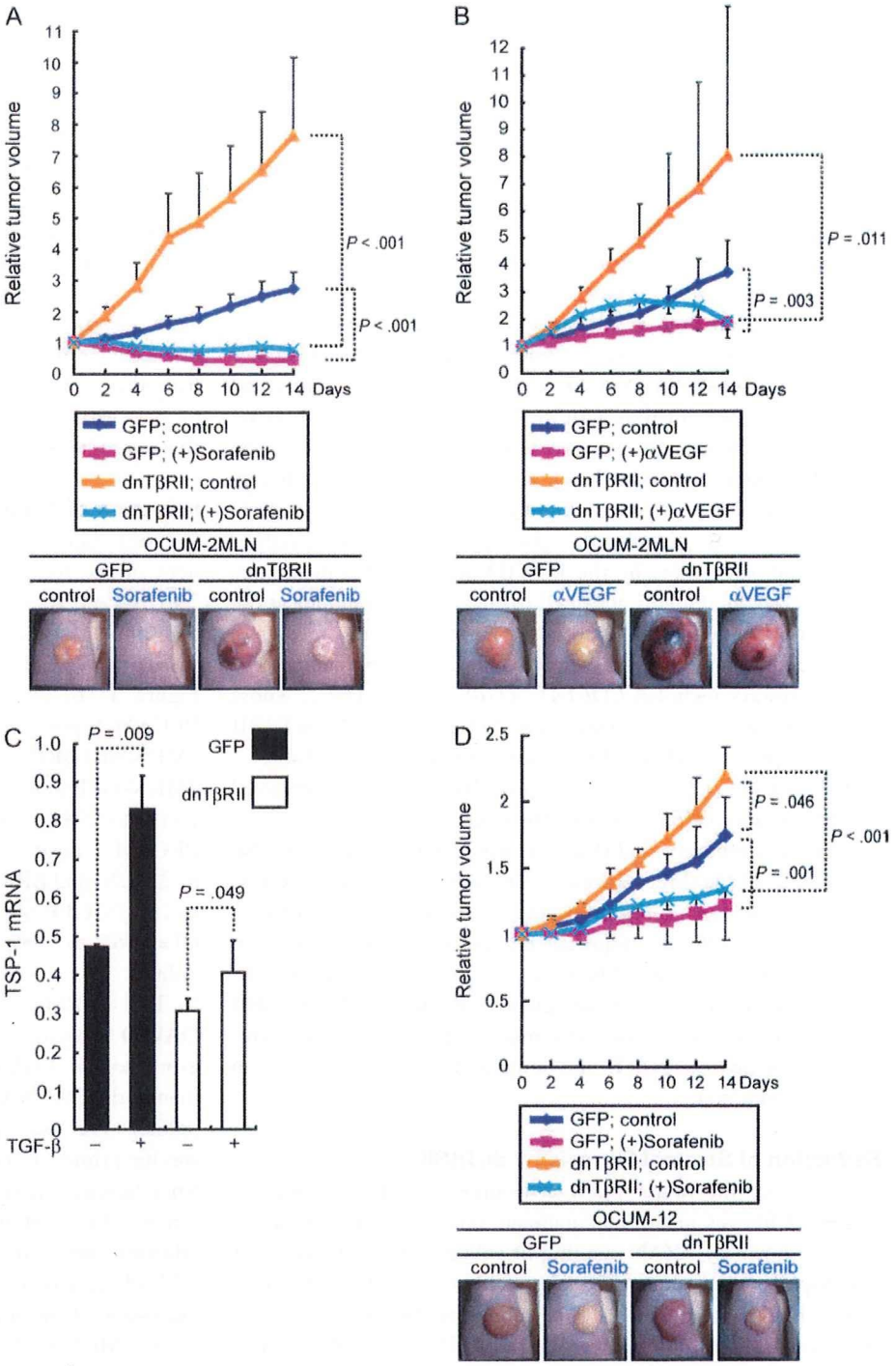

Figure 5. Administration of sorafenib and tumor growth in nude mice. **A)** Growth curve of xenografted 2MLN-GFP and 2MLN-dnTβRII tumors and sorafenib treatment. Mice bearing tumors were treated with 800 μg of sorafenib or with vehicle, as indicated, every day for 14 days (n = 6 mice per group). The representative macroscopic appearance of the tumors at day 7 is shown in the **bottom panels**. **B)** Growth curve of xenografted 2MLN-GFP and 2MLN-dnTβRII tumors in the presence and absence of anti-VEGF neutralizing antibody (n = 6 mice per group). Mice bearing tumors were treated for 14 days with 50 μg of anti-VEGF antibody or vehicle, as indicated, twice a week. The representative macroscopic appearance of the tumors at day 7 is shown in the **bottom panels**. **C)** Expression of human TSP-1 mRNA and treatment with TGF-β. TSP-1 mRNA expression was determined by quantitative real-time reverse transcription–polymerase chain reaction in the control OCUM-12-GFP (GFP) and OCUM-12-dnTβRII (dnTβRII) cells that were treated with TGF-β (1 ng/mL) or left untreated for 24 hours in vitro. The experiment was conducted two times, each sample was assessed in triplicate, and data were averaged. Data from one representative experiment of these are shown. **D)** Growth curves of xenografted OCUM-12-GFP and OCUM-12-dnTβRII tumors and sorafenib treatment. Mice bearing tumors were treated with 800 μg of sorafenib or with vehicle, as indicated, every day for 14 days (n = 7 mice per group). The representative macroscopic appearance of the tumors at day 14 is shown in the **bottom panels**. **Error bars** = 95% confidence intervals. *P* values for (**A**), (**B**), and (**D**) were calculated by two-way repeated measures analysis of variance. Those for (**C**) were calculated with a Student's *t* test, two-sided. DMSO = dimethyl sulfoxide (vehicle). dnTβRII = dominant-negative TGF-β type II receptor; GFP = green fluorescent protein; VEGF = vascular endothelial growth factor; TGF-β = transforming growth factor β; TSP-1 = thrombospondin-1.

immunoblotting. We found that GFP was expressed in the 2MLN-GFP control cells and dnTβRII was expressed in 2MLN-dnTβRII cells (Figure 1, A). In contrast to the parental 2MLN cells and GFP-transfected 2MLN-GFP cells, TGF-β–induced phosphorylated Smad2 was not detected in 2MLN-dnTβRII cells (Figure 1, A). We next used quantitative real-time RT-PCR analysis to show that the induction of Smad7 mRNA, a well-known target of TGF-β signaling, by TGF-β was lower in the 2MLN-dnTβRII cells than in OCUM-2MLN or 2MLN-GFP cells (Figure 1, B). 2MLN, 2MLN-GFP, and 2MLN-dnTβRII cells had similar proliferation rates, and the proliferation rates of these cells were not statistically significantly inhibited after TGF-β treatment (Figure 1, C).

Next, 2MLN-GFP or 2MLN-dnTβRII cells were subcutaneously transplanted into nude mice (n = 8 mice in each group), and tumor size was measured every other day until day 10. Although the proliferation of these cell types did not differ in vitro, the volumes of 2MLN-dnTβRII tumors were statistically significantly larger than those of 2MLN-GFP tumors (Figure 1, D; mean volume on day 10 relative to that on day 0 of 2MLN-dnTβRII tumors = 3.49 and of 2MLN-GFP tumors = 2.46, difference = 1.02, 95% confidence interval [CI] = 0.21 to 1.84; for group effect, *P* = .003;

and for the sampling time effect and the dnTβRII group effect × sampling time effect, $P < .001$, by a two-way repeated measures ANOVA test for tumor growth). We also orthotopically transplanted 2MLN-GFP or 2MLN-dnTβRII cells into the gastric wall of nude mice and determined tumor size on days 14 and 21 after implantation. The relative tumor area of 2MLN-dnTβRII (2.98) was statistically significantly larger than that of 2MLN-GFP (1.59) (Figure 1, E) (difference = 1.39, 95% CI = 0.87 to 1.91; $P < .001$, n = 8 mice in each group).

To explore factors responsible for the increased growth of the 2MLN-dnTβRII tumors in vivo, we used microarray analysis to identify differentially expressed human genes in the subcutaneously transplanted 2MLN-GFP and 2MLN-TβRII tumors and then used pathway analysis with the DAVID program to annotate the list of differentially expressed genes in these tumors. The DAVID program provides batch annotation and gene ontology term enrichment analysis to highlight the most relevant gene ontology terms associated with a given gene list (26). The analysis of our microarray data by the DAVID program identified three pathways as differentially activated pathways: cell communication, interactions between the extracellular matrix and the receptors, and focal adhesion (Supplementary Table 2, available online). All three pathways included *COL1A1*, *THBS1*, and *LAMC2*, whose expression levels were substantially lower in 2MLN-dnTβRII tumors than in 2MLN-GFP tumors (Supplementary Table 2, available online). *COL1A1* encodes procollagen I, which is involved in fibrosis, and *THBS1* encodes thrombospondin-1, which is an angiogenesis inhibitor. *LAMC2* encodes laminin-γ2 and was also included in all the three pathways. Although the increased expression of laminin-γ2 has been reported to be involved in invasion of certain cancers (28), the importance of its decreased expression in cancer remains unknown. Therefore, we further analyzed the relationship between the increased growth of the 2MLN-dnTβRII tumors and tumor microenvironment, especially fibrosis, with a focus on procollagen I, and angiogenesis, with a focus on thrombospondin-1.

Reduction of Stromal Fibrosis by dnTβRII

We analyzed the tumor microenvironment by determining the degree of fibrosis in the subcutaneous and orthotopic tumor tissues, as shown by AZAN staining of collagen fibers (Figure 2, A and Supplementary Figure 1, A, available online). In both tumor types, the area of fibrosis as determined by AZAN staining was statistically significantly lower in the 2MLN-dnTβRII tumors than in the 2MLN-GFP tumors (for subcutaneous tumors, 2MLN-dnTβRII had 6.1% and 2MLN-GFP had 30.1% [n = 9 mice per group], difference = 24.0%, 95% CI = 14.4% to 33.6%, $P < .001$; and for orthotopic tumors, 2MLN-dnTβRII tumors had 19.8% and 2MLN-GFP tumors had 47.0%, n = 9, difference = 27.2%, 95% CI = 20.0% to 34.4%, $P < .001$).

Microarray analysis revealed that the COL1A1 expression was lower in the 2MLN-dnTβRII tumors than in the 2MLN-GFP tumors. These results were validated with quantitative real-time RT-PCR with human COL1A1–specific primers and subcutaneous tumor samples (expression in 2MLN-dnTβRII tumors was 1.01 arbitrary units and that in 2MLN-GFP tumors was 17.46 arbitrary units, n = 3, difference = 16.4, 95% CI = 12.3 to 20.6 arbitrary units, $P < .001$) (Figure 2, B, left panel). In the same tumors, expression of the mouse Col1A1 mRNA was similar in 2MLN-dnTβRII and 2MLN-GFP tumors (Figure 2, B, middle panel; $P = .026$). In cultured cells, expression of the human COL1A1 mRNA was induced by TGF-β in the 2MLN-GFP cells but not in the 2MLN-dnTβRII cells (Figure 2, B, right panel). Secretion of TGF-β1 as determined by an enzyme-linked immunosorbent assay revealed that production of TGF-β1 was lower in 2MLN-dnTβRII cells (22.1 pg/mL) than in 2MLN-GFP cells (552.4 pg/mL) (difference = 530.3 pg/mL, 95% CI = 502.7 to 558.0 pg/mL, $P < .001$) (Figure 2, C). Thus, the material in the extracellular matrix in these tumors appears to be derived primarily from the gastric carcinoma cells and that the increased production of these extracellular matrix materials may be induced by TGF-β1 that is produced by the gastric carcinoma cells.

Induction of Tumor Angiogenesis by dnTβRII

We next examined tumor angiogenesis, another important component of the tumor microenvironment, in 2MLN-dnTβRII and 2MLN-GFP tumors in vivo. We used immunohistochemistry to determine vascular density in tumors with a specific marker of vascular endothelium, PECAM-1 (Figure 2, D and Supplementary Figure 1, B, available online). In subcutaneous tumors, the PECAM-1–positive area was statistically significantly higher in 2MLN-dnTβRII tumors (8.91% per microscopic field) than in 2MLN-GFP tumors (4.78%) (n = 6, difference = 4.13%, 95% CI = 1.31% to 6.94%; $P = .008$) (Figure 2, D). In orthotopic tumors, the PECAM-1–positive area was also statistically significantly higher in 2MLN-dnTβRII tumors (1.95% per microscopic field) than in 2MLN-GFP tumors (0.27%) (n = 7, difference = 1.67%, 95% CI = 0.46% to 2.88%; $P = .013$) (Supplementary Figure 1, B, available online).

The *THBS1* gene was included in all pathways selected by DAVID analysis, and the microarray analysis showed that the expression of THBS1 was lower in the 2MLN-dnTβRII tumors than in the 2MLN-GFP tumors (Supplementary Table 2, available online). We used quantitative RT-PCR with human THBS1–specific primers to confirm that the expression of THBS1 mRNA from human carcinoma cells was lower in the 2MLN-dnTβRII tumors (0.13 arbitrary unit) than in the 2MLN-GFP tumors (2.20 arbitrary units) (difference = 2.07 arbitrary units, 95% CI = 1.92 to 2.22 arbitrary units; $P < .001$) (Figure 2, E, left panel). Moreover, expression of thrombospondin-1 was potently induced by TGF-β in the 2MLN-GFP cells in vitro but not in the 2MLN-dnTβRII cells (Figure 2, E, right panel). In addition to thrombospondin-1, VEGF has been reported to be involved in angiogenesis in the Smad4-deficient pancreatic tumor model (29). However, the level of VEGF expression, as determined with primers specific for both human and mouse VEGF, was similar between 2MLN-GFP and 2MLN-dnTβRII cells in vivo and in vitro (data not shown), indicating that decreased expression of thrombospondin-1 may be involved in the enhanced angiogenesis in the 2MLN-dnTβRII tumors.

Phenotype of Tumors Containing a Mixture of Both 2MLN-GFP and 2MLN-dnTβRII Cells

The results described above strongly suggest that regulation of structural elements in the tumor microenvironment by TGF-β

signaling may be important to tumor formation in diffuse-type gastric carcinomas; however, it is still possible that the changes in tumor growth rate may be induced by other autonomous factor(s) in the cancer cells. To investigate further whether the tumor microenvironment serves as a major determinant of tumor growth in this model, we mixed equal amounts of the 2MLN-GFP and 2MLN-dnTβRII cells and transplanted the cell mixture into nude mice (Figure 3, A). If the tumor microenvironment plays a major role in tumor growth, then the 2MLN-GFP+dnTβRII tumors should contain equal number of both cell types (Figure 3, A). In contrast, if the 2MLN-dnTβRII portion of the tumor grows faster in cell-autonomous fashion, then the 2MLN-GFP+dnTβRII tumors should be composed mainly of 2MLN-dnTβRII cells. Histological examination of 2MLN-GFP+dnTβRII tumors with GFP fluorescence and by use of hemagglutinin antibody to detect the 2MLN-GFP and 2MLN-dnTβRII cells, respectively, revealed that the 2MLN-GFP+dnTβRII tumors contain almost equal number of the two cell types ($P = .56$) (Figure 3, B). We also examined angiogenesis in 2MLN-GFP+dnTβRII tumors by use of PECAM-1 immunostaining and found that the level of vascular density in the mixed-cell tumor (2.61% per microscopic field) was intermediate between that of 2MLN-dnTβRII tumors (4.22%) and 2MLN-GFP tumors (1.34%) (difference with 2MLN-dnTβRII tumors = 1.61, 95% CI = 0.37% to 2.86%, $P = .023$ [n = 3]; difference with 2MLN-GFP tumors = 1.27%, 95% CI = 0.73% to 1.81%, $P = .003$ [n = 3]) (Figure 3, C).

Inhibition of Angiogenesis and Growth of 2MLN-dnTβRII Tumors

To determine whether decreased thrombospondin-1 expression is involved in the accelerated proliferation of 2MLN-dnTβRII tumors, we used a lentivirus system to introduce the gene for thrombospondin-1 into the 2MLN-dnTβRII cells, and these cells were injected into mice to form tumors. At day 7, the volume of 2MLN-dnTβRII tumors that expressed exogenous thrombospondin-1 (3.08×10^3 mm^3) was lower than that of 2MLN-dnTβRII tumors alone (12.0×10^3 mm^3) (difference = 8.94×10^3 mm^3, 95% CI = 5.82×10^3 to 12.1×10^3 mm^3, $P < .001$ [n = 6]) and was similar to that of control 2MLN-GFP tumors that expressed GFP (2.81×10^3 mm^3; difference = 0.27×10^3 mm^3, 95% CI = -1.67×10^3 to 2.21×10^3 mm^3, $P = .76$ [n = 6]) (Figure 4, A). Immunostaining of the tumors with an antibody against PECAM-1 protein demonstrated that the vascular density of the 2MLN-dnTβRII tumors was reduced by the introduction of thrombospondin-1 (1.90% per microscopic field) compared with that of 2MLN-dnTβRII tumors alone (7.74%; difference = 5.84%, 95% CI = 4.21% to 7.48%, $P < .001$ [n = 3]) or that of 2MLN-GFP tumors as control (1.85% per microscopic field; difference = 0.05%, 95% CI = −1.64% to 1.73%, $P = .9$ [n = 3]) (Figure 4, B). In contrast, AZAN staining showed that the degree of fibrosis was not statistically significantly changed by introduction of thrombospondin-1 (Figure 4, C).

We obtained additional support for the finding that decrease in thrombospondin-1 is involved in the accelerated growth of the 2MLN-dnTβRII tumors by knocking down the expression of thrombospondin-1 in the 2MLN-GFP cells with an RNA interference approach. The 2MLN-GFP cells expressing the microRNA construct against thrombospondin-1 were termed 2MLN-GFP+miTSP-1 cells. Expression of thrombospondin-1 was lower in the 2MLN-GFP+miTSP-1 cells than in 2MLN-GFP cells in vitro (Figure 4, D). When these cells were inoculated to mice to form tumors, knockdown of thrombospondin-1 resulted in the volumes of 2MLN-GFP+miTSP-1 tumors being larger than those of 2MLN-GFP tumors (Figure 4, E; mean volume of 2MLN-GFP+miTSP-1 tumor on day 14 relative to that on day 0 after starting evaluation = 4.91 and that of 2MLN-GFP tumor = 3.79; difference = 1.12, 95% CI = 0.80 to 1.44; for group effect, sampling time effect, and group effect × sampling time effect, $P < .001$, by a two-way repeated measures ANOVA test for tumor growth [n = 6 in each group]). In addition, 2MLN-GFP+miTSP-1 tumors were smaller than 2MLN-dnTβRII tumors (Figure 4, E; volume of 2MLN-GFP+miTSP-1 tumor on day 14 relative to that on day 0 after starting evaluation = 4.91 and that of 2MLN-dnTβRII tumor = 5.65; difference = 0.74, 95% CI = −0.78 to 2.27; the result of a two-way repeated measures ANOVA test for the tumor growth from days 0 to 14 [n = 6 in each group] for group effect, $P = .010$; for sampling time effect, $P < .001$; for group effect × sampling time effect, $P = .025$), in agreement with the finding that the in vivo expression level of thrombospondin-1 mRNA in the 2MLN-GFP+miTSP-1 tumors (0.42) was higher than that of the 2MLN-dnTβRII tumors (0.12; difference = 0.30, 95% CI = 0.12 to 0.49; $P = .011$) (Figure 4, F).

To further elucidate the contribution of enhanced angiogenesis to increased tumor growth in the gastric carcinoma model, we treated the tumor-bearing mice with sorafenib, a small-molecule inhibitor of various tyrosine kinases, including VEGF receptor-2, Raf, and platelet-derived growth factor receptor (30,31). Sorafenib (40 mg/kg) or a vehicle control was intraperitoneally administered into the tumor-bearing mice every day (n = 6 mice per group). Treatment with sorafenib strongly suppressed the growth of both 2MLN-GFP tumors (Figure 5, A; tumor volume in treated mice on day 14 relative to that on day 0 after starting evaluation = 0.45 and that in untreated mice = 2.73; difference = 2.28, 95% CI = 1.81 to 2.76; for group effect, sampling time effect, and group effect × sampling time effect, $P < .001$, by a two-way repeated measures ANOVA test for tumor growth) and 2MLN-dnTβRII tumors (Figure 5, A; tumor volume in treated mice on day 14 relative to that on day 0 after starting evaluation = 0.79 and that in untreated mice = 7.64; difference = 6.85, 95% CI = 4.34 to 9.37; for group effect, sampling time effect, and group effect × sampling time effect, $P < .001$, by a two-way repeated measures ANOVA test for tumor growth). The tumors treated with sorafenib were pale in comparison with the untreated tumors, indicating the reduction of tumor vasculature and thus hemoglobin. To further confirm the effects of inhibition of angiogenesis on the tumor growth, an anti-VEGF neutralizing antibody (2.5 mg/kg) or a vehicle control was intraperitoneally administered into the tumor-bearing mice twice a week (n = 8 mice per group). As with sorafenib treatment, treatment with the anti-VEGF neutralizing antibody reduced the volume of both 2MLN-GFP tumors (Figure 5, B; tumor volume in treated mice on day 14 relative to that on day 0 after starting evaluation = 1.89 and that in control treated mice = 3.72; difference = 1.83, 95% CI = 0.68 to 2.98; for group effect, $P = .003$; and for sampling time effect and group effect × sampling time effect, $P < .001$, by a two-way repeated measures ANOVA test for tumor growth) and 2MLN-dnTβRII

tumors (Figure 5, B; tumor volume in treated mice on day 14 relative to that on day 0 after starting evaluation = 1.90 and that in control treated mice = 8.05; difference = 6.15, 95% CI = 0.12 to 12.18; for group effect, $P = .011$; and for sampling time effect and group effect × sampling time effect, $P < .001$, by a two-way repeated measures ANOVA test for tumor growth).

Disruption of TGF-β Signaling in Another Diffuse-Type Gastric Carcinoma Cell Line

In addition to OCUM-2MLN cells, we also used another diffuse-type gastric carcinoma cell line, OCUM-12, to investigate the effects of disruption of TGF-β signaling. TGF-β induced phosphorylation of Smad2 (Supplementary Figure 2, A, available online) and inhibited the proliferation of OCUM-12 cells in vitro (Supplementary Figure 2, B, available online), indicating that this cell line also responds to TGF-β. To further examine the effects of disrupting TGF-β signaling in this cell line, we generated OCUM-12 cells expressing GFP or dnTβRII and used them to confirm that phosphorylation of Smad2 was attenuated in OCUM-12-dnTβRII cells (Supplementary Figure 2, A, available online). We found that TGF-β1–induced thrombospondin-1 expression was attenuated in the OCUM-12-dnTβRII cells as it was in 2MLN-dnTβRII cells (Figure 5, C). Moreover, the volume of the OCUM-12 tumors expressing dnTβRII was statistically significantly larger than that of OCUM-12-GFP tumors (Figure 5, D; volume of OCUM-12-dnTβRII tumor on day 14 relative to that on day 0 after starting evaluation = 2.19 and that of OCUM-12-GFP tumor = 1.80; difference = 0.39, 95% CI = 0.014 to 0.772; for group effect, $P = .046$; for sampling time effect, $P < .001$; for group effect × sampling time effect, $P = .003$, by a two-way repeated measures ANOVA test for tumor growth [n = 7 mice in each group]), and sorafenib reduced the volume of both OCUM-12-GFP tumors (volume of treated tumor on day 14 relative to that on day 0 after starting evaluation = 1.17 and that of untreated tumor = 1.80; difference = 0.63, 95% CI = 0.28 to 0.98; for group effect, $P = .001$; and for sampling time effect and group effect × sampling time effect, $P < .001$, by a two-way repeated measures ANOVA test for tumor growth [n = 7 mice in each group]) and OCUM-12-dnTβRII tumors (volume of treated tumor on day 14 relative to that on day 0 after starting evaluation = 1.36 and that of untreated tumor = 2.19; difference = 0.83, 95% CI = 0.51 to 1.15; for group effect, $P < .001$; for sampling time effect and group effect × sampling time effect, $P < .001$, by a two-way repeated measures ANOVA test for tumor growth [n = 7 mice in each group]).

Expression of Thrombospondin-1 and Phosphorylated Smad2 in Human Gastric Carcinoma Tissues

Finally, we examined the status of TGF-β signaling in human gastric tumor tissues by use of antibody against phosphorylated Smad2 and the level of expression of thrombospondin-1 with antibody against thrombospondin-1. Both phosphorylated Smad2 and thrombospondin-1 were detected in normal epithelium adjacent to tumor (data not shown) and in some diffuse- and intestinal-type gastric cancer tissues (Supplementary Figure 3, A, available online). Immunostaining of 102 human gastric cancer specimens revealed that 44 (43%) tumors expressed both phosphorylated Smad2 and thrombospondin-1 and that 24 (23%) expressed neither (Supplementary Table 3, available online). Furthermore, a positive association was observed between the expression of thrombospondin-1 and of phosphorylated Smad2 ($P = .002$; Supplementary Table 3, available online). We also found that some cancer cells had weaker staining of phosphorylated Smad2 associated with weaker staining of thrombospondin-1 and that these cells were adjacent to cancer cells with strongly positive staining of phosphorylated Smad2 and strongly positive thrombospondin-1 (Supplementary Figure 3, B, available online). This observation suggested that the level of expression of thrombospondin-1 may be associated with the level of TGF-β signaling in each cancer cell, which varied even in the same tumor tissue.

Discussion

We demonstrated in this study that disruption of TGF-β signaling in diffuse-type gastric carcinoma models appears to accelerate the progression of cancer, as shown by increased growth of the 2MLN-dnTβRII tumors compared with that of the control 2MLN-GFP tumors in the subcutaneous and orthotopic transplantation models. Furthermore, microarray analysis of gene expression revealed decreased production of thrombospondin-1 in the 2MLN-dnTβRII tumors. Overexpression of thrombospondin-1 suppressed the growth of OCUM-2MLN tumors, but knockdown of thrombospondin-1 expression stimulated tumor growth. Moreover, we have also demonstrated that regulation of angiogenesis by sorafenib or anti-VEGF antibody efficiently prevented the growth of tumors in vivo.

Systemic administration of TGF-β inhibitors has been shown to suppress growth and metastasis of some tumors by acting on cancer cells and the tumor microenvironment (32,33). However, we found that disruption of TGF-β signaling in diffuse-type gastric carcinoma cells accelerated tumor formation. We found, in experiments with a mixture of the wild-type OCUM-2MLN cells and OCUM-2MLN cells expressing dnTβRII, that the increased growth of 2MLN-dnTβRII tumors appeared to be mainly attributable to alterations in the tumor microenvironment, not to autonomous properties of the cancer cells. The tumor microenvironment, which has been reported to be important during tumor progression (6), contains many structural elements, including blood vessels and fibrotic tissues. Consistently, we found that absence of TGF-β–induced expression of thrombospondin-1, an angiogenic inhibitor, is associated with increased growth of dnTβRII tumors in vivo, indicating that increased angiogenesis in the dnTβRII-expressing tumors appears to be important in the accelerated growth of such tumors.

TGF-β binds to TβRII and TGF-β type I receptorand activates Smad2 and Smad3, which transduce signals by complexing with Smad4. Decreased expression of TβRII, Smad2, and Smad4, or loss-of-function mutations in at least one of these genes, has been reported in various cancers at advanced stages, including breast cancer and colon cancer (16). Decreased expression of Smad4 has been observed in many clinical specimens of diffuse-type gastric carcinoma (20,34). Although mutations in TβRII have not been reported in diffuse-type gastric carcinoma, these findings indicate that disruption of TGF-β signaling may accelerate the progression of this type of cancer at advanced stages.

Schwarte-Waldhoff et al. (29) reported that the lack of Smad4 in an experimental pancreatic cancer model stimulated secretion of VEGF, repressed the expression of thrombospondin-1, and led to increased angiogenesis and tumor growth. Our microarray data revealed that although expression of VEGF was not statistically significantly altered in the 2MLN-dnTβRII tumors, compared with the 2MLN-GFP tumors, expression of thrombospondin-1 was reduced. Moreover, we found that the expression of thrombospondin-1 was induced by TGF-β in the OCUM-2MLN cells but not in the 2MLN-dnTβRII cells, in agreement with previous reports on the induction of thrombospondin-1 by TGF-β in certain cell types, including hepatic HuH-7 cells, osteosarcoma MG63 cells, and rat tubular epithelial cells (35,36). We obtained similar results with another diffuse-type gastric carcinoma cell line, OCUM-12. Furthermore, we found that expression of thrombospondin-1 reduced the growth of 2MLN-dnTβRII tumors in mice and that growth of tumors produced from 2MLN-GFP cells in which thrombospondin-1 expression had been inhibited was accelerated. Moreover, the association that we found between the expression of phosphorylated Smad2 and thrombospondin-1 indicated that attenuation or loss of TGF-β signaling results in decreased expression of thrombospondin-1 in human gastric cancer tissues. Thrombospondin-1 has been shown to inhibit growth and differentiation of endothelial cells and to induce their apoptosis (24,25). Thus, the decreased level of thrombospondin-1 in these tumor models appears to accelerate tumor angiogenesis.

The importance of tumor angiogenesis in the accelerated growth of the 2MLN-dnTβRII tumors was further supported by the potent inhibition of tumor growth by treatment with sorafenib, regardless of the status of TGF-β signaling in the cancer cells. Sorafenib was effective not only in OCUM-2MLN tumors but also in OCUM-12 tumors, although the latter were relatively resistant to sorafenib's growth inhibitory effect in vitro (A. Komuro, M. R. Kano and K. Miyazono, University of Tokyo, M. Yashiro and K. Hirakawa, Osaka City University, unpublished data; the 50% inhibitory concentration [IC_{50}] in OCUM-2MLN cells = 1.45 μM and in OCUM-12 cells = 8.75 μM). Thus, the effect of sorafenib on the gastric tumor models in vivo may be mostly due to suppression of tumor angiogenesis, although direct effects of sorafenib on the gastric carcinoma cells may also contribute to its growth inhibitory effect in vivo. In accordance with these results, we found that an anti-VEGF neutralizing antibody effectively reduced the growth of OCUM-2MLN tumors.

Our study had several limitations. Although we examined the growth of diffuse-type gastric carcinoma in subcutaneous and orthotopic transplantation models, the experiments were conducted with immunocompromised mice. Immune function may affect the growth of diffuse-type gastric carcinoma in human patients. Furthermore, we analyzed the growth of primary tumors but not the metastasis of tumors. The question of whether TGF-β signaling regulates metastasis in a cancer cell–autonomous fashion or in a microenvironment-dependent manner should be explored in the future.

In conclusion, we have shown that disruption of TGF-β signaling in a mouse model of diffuse-type gastric carcinoma, which may be analogous to what occurs during progression of this disease in humans, promotes tumorigenesis by accelerating angiogenesis. Because the loss of TβRII or Smad4 expression has been reported to induce tumor angiogenesis in other types of cancers (29,37), the administration of angiogenesis inhibitors, including sorafenib and thrombospondin-1 analogues (38), may be useful as a treatment for those cancers with disrupted TGF-β signaling pathways.

References

1. Crew KD, Neugut AI. Epidemiology of gastric cancer. *World J Gastroenterol.* 2006;12(3):354–362.
2. Hohenberger P, Gretschel S. Gastric cancer. *Lancet.* 2003;362(9380):305–315.
3. Laurén P. The two histological main types of gastric carcinoma: diffuse and so-called intestinal-type carcinoma. *Acta Pathol Microbiol Scand.* 1965;64:31–49.
4. Yashiro M, Chung YS, Nishimura S, Inoue T, Sowa M. Establishment of two new scirrhous gastric cancer cell lines: analysis of factors associated with disseminated metastasis. *Br J Cancer.* 1995;72(5):1200–1210.
5. Henson DE, Dittus C, Younes M, Nguyen H, Albores-Saavedra J. Differential trends in the intestinal and diffuse types of gastric carcinoma in the United States, 1973–2000. *Arch Pathol Lab Med.* 2004;128(7):765–770.
6. Bierie B, Moses HL. TGF-β and the tumor microenvironment. In: Derynck R, Miyazono K, eds. *The TGF-β Family.* New York, NY: Cold Spring Harbor Laboratory Press; 2008:965–987.
7. Feng XH, Derynck R. Specificity and versatility in TGF-β signaling through Smads. *Annu Rev Cell Dev Biol.* 2005;21:659–693.
8. Shi Y, Massagué J. Mechanisms of TGF-β signaling from cell membrane to the nucleus. *Cell.* 2003;113(6):685–700.
9. Roberts AB, Wakefield LM. The two faces of transforming growth factor β in carcinogenesis. *Proc Natl Acad Sci USA.* 2003;100(15):8621–8623.
10. Moustakas A, Heldin CH. Signaling networks guiding epithelial-mesenchymal transitions during embryogenesis and cancer progression. *Cancer Sci.* 2007;98(10):1512–1520.
11. Akhurst RJ. TGF-β signaling in epithelial-mesenchymal transition and invasion and metastasis. In: Derynck R, Miyazono K, eds. *The TGF-β Family.* New York, NY: Cold Spring Harbor Laboratory Press; 2008:939–964.
12. Yin JJ, Selander K, Chirgwin JM, et al. TGF-β signaling blockade inhibits PTHrP secretion by breast cancer cells and bone metastases development. *J Clin Invest.* 1999;103(2):197–206.
13. Muraoka RS, Dumont N, Ritter CA, et al. Blockade of TGF-β inhibits mammary tumor cell viability, migration, and metastases. *J Clin Invest.* 2002;109(12):1551–1559.
14. Yang YA, Dukhanina O, Tang B, et al. Lifetime exposure to a soluble TGF-β antagonist protects mice against metastasis without adverse side effects. *J Clin Invest.* 2002;109(12):1607–1615.
15. Azuma H, Ehata S, Miyazaki H, et al. Effect of Smad7 expression on metastasis of mouse mammary carcinoma JygMC(A) cells. *J Natl Cancer Inst.* 2005;97(23):1734–1746.
16. Lahn M, Berry B, Kloeker S, Yingling JM. TGF-β receptor kinase inhibitors for the treatment of cancer. In: ten Dijke P, Heldin CH, eds. *Smad Signal Transduction.* New York, NY: Springer Verlag; 2006:415–442.
17. Mizoi T, Ohtani H, Miyazono K, et al. Immunoelectron microscopic localization of transforming growth factor β1 and latent transforming growth factor β1 binding protein in human gastrointestinal carcinomas: qualitative difference between cancer cells and stromal cells. *Cancer Res.* 1993;53(1):183–190.
18. Kinugasa S, Abe S, Tachibana M, et al. Overexpression of transforming growth factor-β1 in scirrhous carcinoma of the stomach correlates with decreased survival. *Oncology.* 1998;55(6):582–587.
19. Vagenas K, Spyropoulos C, Gavala V, Tsamandas AC. TGFβ1, TGFβ2, and TGFβ3 protein expression in gastric carcinomas: correlation with prognostics factors and patient survival. *J Surg Res.* 2007;139(2):182–188.
20. Kim JY, Park DY, Kim GH, et al. Smad4 expression in gastric adenoma and adenocarcinoma: frequent loss of expression in diffuse type of gastric adenocarcinoma. *Histol Histopathol.* 2005;20(2):543–549.
21. Fujihara T, Sawada T, Hirakawa K, et al. Establishment of lymph node metastatic model for human gastric cancer in nude mice and analysis of factors associated with metastasis. *Clin Exp Metastasis.* 1998;16(4):389–398.

22. Qiu H, Yashiro M, Shinto O, Matsuzaki T, Hirakawa K. DNA methyltransferase inhibitor 5-aza-CdR enhances the radiosensitivity of gastric cancer cells. *Cancer Sci.* 2009;100(1):181–188.
23. Shibuya K, Shirakawa J, Kameyama T, et al. CD226 (DNAM-1) is involved in lymphocyte function-associated antigen 1 costimulatory signal for naive T cell differentiation and proliferation. *J Exp Med.* 2003;198(12):1829–1839.
24. Yamauchi M, Imajoh-Ohmi S, Shibuya M. Novel antiangiogenic pathway of thrombospondin-1 mediated by suppression of the cell cycle. *Cancer Sci.* 2007;98(9):1491–1497.
25. Jiménez B, Volpert OV, Crawford SE, Febbraio M, Silverstein RL, Bouck N. Signals leading to apoptosis-dependent inhibition of neovascularization by thrombospondin-1. *Nat Med.* 2000;6(1):41–48.
26. Dennis G Jr, Sherman BT, Hosack DA, et al. DAVID: Database for Annotation, Visualization, and Integrated Discovery. *Genome Biol.* 2003;4(5):P3.
27. Zhang J, Ito R, Oue N, et al. Expression of thrombospondin-1 is correlated with microvessel density in gastric carcinoma. *Virchows Archiv.* 2004;442(6):563–568.
28. Eguchi T, Inoue T, Fujii K, et al. Laminin-5 (gamma2 chain) is a marker of invading cancer cells in human gallbladder carcinoma: special emphasis on extension of carcinoma in situ along Rokitansky-Aschoff sinuses. *Oncol Rep.* 2008;20(1):33–39.
29. Schwarte-Waldhoff I, Volpert OV, Bouck NP, et al. Smad4/DPC4-mediated tumor suppression through suppression of angiogenesis. *Proc Natl Acad Sci USA.* 2000;97(17):9624–9629.
30. Wilhelm S, Carter C, Lynch M, et al. Discovery and development of sorafenib: a multikinase inhibitor for treating cancer. *Nat Rev Drug Discov.* 2006;5(10):835–844.
31. Liu L, Cao Y, Chen C, et al. Sorafenib blocks the RAF/MEK/ERK pathway, inhibits tumor angiogenesis, and induces tumor cell apoptosis in hepatocellular carcinoma model PLC/PRF/5. *Cancer Res.* 2006;66(24):11851–11858.
32. Nam JS, Terabe M, Mamura M, et al. An anti-transforming growth factor β antibody suppresses metastasis via cooperative effects on multiple cell compartments. *Cancer Res.* 2008;68(10):3835–3843.
33. Kawajiri H, Yashiro M, Shinto O, et al. A novel transforming growth factor β receptor kinase inhibitor, A-77, prevents the peritoneal dissemination of scirrhous gastric carcinoma. *Clin Cancer Res.* 2008;14(9):2850–2860.
34. Okano H, Shinohara H, Miyamoto A, Takaori K, Tanigawa N. Concomitant overexpression of cyclooxygenase-2 in HER-2-positive on Smad4-reduced human gastric carcinomas is associated with a poor patient outcome. *Clin Cancer Res.* 2004;10(20):6938–6945.
35. Okamoto M, Ono M, Uchiumi T, et al. Up-regulation of thrombospondin-1 gene by epidermal growth factor and transforming growth factor β in human cancer cells—transcriptional activation and messenger RNA stabilization. *Biochim Biophys Acta.* 2002;1574(1):24–34.
36. Nakagawa T, Lan HY, Glushakova O, et al. Role of ERK1/2 and p38 mitogen-activated protein kinases in the regulation of thrombospondin-1 by TGF-β1 in rat proximal tubular cells and mouse fibroblasts. *J Am Soc Nephrol.* 2005;16(4):899–904.
37. Lu SL, Herrington H, Reh D, et al. Loss of transforming growth factor-β type II receptor promotes metastatic head-and-neck squamous cell carcinoma. *Genes Dev.* 2006;20(10):1331–1342.
38. Ebbinghaus S, Hussain M, Tannir N, et al. Phase 2 study of ABT-510 in patients with previously untreated advanced renal cell carcinoma. *Clin Cancer Res.* 2007;13(22 Pt 1):6689–6695.

Funding

KAKENHI (Grant-in-Aid for Scientific Research; Project No. 17016011) from the Ministry of Education, Culture, Sports, Science, and Technology of Japan.

Notes

The study sponsors had no role in the design of the study or in the collection, analysis, or interpretation of the data. The authors take full responsibility for the study design, data collection, analysis and interpretation of the data, the decision to submit the manuscript for publication, and the writing of the manuscript.
We are grateful to Masako Oka for discussion, and Hiroko Yanagisawa, Makoto Arai, Saori Sakaue, and Satoru Yonekura for technical assistance.

Manuscript received August 6, 2008; revised January 28, 2009; accepted February 20, 2009.

Comparison of the effects of the kinase inhibitors imatinib, sorafenib, and transforming growth factor-β receptor inhibitor on extravasation of nanoparticles from neovasculature

Mitsunobu R. Kano,[1,2,3,4] Yukari Komuta,[1,5] Caname Iwata,[1] Masako Oka,[1] Yo-taro Shirai,[1] Yasuyuki Morishita,[1] Yasuyoshi Ouchi,[4] Kazunori Kataoka[2] and Kohei Miyazono[1,2,6]

[1]Department of Molecular Pathology, Graduate School of Medicine, University of Tokyo, 7-3-1 Hongo, Bunkyo-ku, Tokyo, 113-0033; [2]Center for Nano-Bio Integration, University of Tokyo, Tokyo, 113-8656; [3]Medical Scientist Training Program, Faculty of Medicine, University of Tokyo, Tokyo, 113-0033; [4]Department of Geriatrics, Graduate School of Medicine, University of Tokyo, 7-3-1 Hongo, Bunkyo-ku, Tokyo, 113-0033; [5]Japan Association for the Advancement of Medical Equipment, 3-42-6 Hongo, Bunkyo-ku, Tokyo, 113-0033, Japan

(Received May 20, 2008/Revised September 11, 2008/Accepted September 14, 2008/Online publication November 25, 2008)

There are a number of kinase inhibitors that regulate components of the neovasculature. We previously reported the use of transforming growth factor (TGF)-β inhibitor on neovasculature in stroma-rich tumor models to increase the intratumoral distribution of nanoparticles. Here, we compared the effects of two other kinase inhibitors, imatinib and sorafenib, with TGF-β inhibitor (LY364947) on extravasation of a modeled nanoparticle, 2 MDa dextran. We first used a mouse model of neoangiogenesis, the Matrigel plug assay, to compare neovasculature formed inside of and around Matrigel plugs (intraplug and periplug regions, respectively). Intraplug vasculature was more strongly pericyte covered, whereas periplug vasculature was less covered. In this model, TGF-β inhibitor exhibited the most potent effect on intraplug vasculature in increasing the extravasation of dextran, whereas sorafenib had the strongest effect on periplug vasculature. Although imatinib and TGF-β inhibitor each reduced pericyte coverage, imatinib also reduced the density of endothelium, resulting in a decrease in overall delivery of nanoparticles. These findings were confirmed in two tumor models, the CT26 colon cancer model and the BxPC3 pancreatic cancer model. The vasculature phenotype in the CT26 model resembled that in the periplug region, whereas the latter resembled that in the intraplug region. Consistent with this, sorafenib most potently enhanced the accumulation of nanoparticles in the CT26 model, whereas TGF-β inhibitor did in the BxPC3 model. In conclusion, the appropriate strategy for optimization of tumor vasculature for nanoparticles may differ depending on tumor type, and in particular on the degree of pericyte coverage around the vasculature. (*Cancer Sci* 2009; 100: 173–180)

The effectiveness of drug delivery into tumor tissues is an important issue in the treatment of solid tumors, in addition to the efficacy of drugs in treating tumor cells. For example, gemcitabine, a first-line anticancer agent for pancreatic adenocarcinoma, exhibited potent *in vitro* growth-inhibitory effects on a cultured cell line derived from the human pancreatic adenocarcinoma line BxPC3.[1] However, it exhibited only slight inhibitory effects on xenografted BxPC3 tumors in mice[2] and slight elongation of survival time in tumor-bearing patients, with significant effects only in the improvement of quality of life index in clinical trials.[3]

Many factors might potentially explain this discrepancy, particularly those related to tumor stroma.[4] Among them, tumor vasculature plays an important role in the delivery of anticancer agents. Extravasation of drugs to tumor tissue constitutes an essential part of drug delivery to tumor tissues,[5] whereas the molecular size of compounds is another important determinant of accumulation.[6] We have recently shown that increased leakiness in tumor neovasculature improves the accumulation of nanoparticles in tumor tissues in animal models of pancreatic adenocarcinoma and diffuse-type advanced gastric cancer.[7] In that study, inhibition of transforming growth factor (TGF)-β signaling reduced pericyte coverage and slightly increased endothelial area, resulting in an increase in vascular leakiness without loss of blood flow. However, numerous studies of tumor neovasculature have shown that it is leaky by nature, and that manipulation of vessels to make them less leaky, or induction of vascular normalization, may therefore benefit drug delivery to tumor tissues.[8] This theory has been supported with the use of vascular endothelial growth factor (VEGF) inhibitors. There are a number of VEGF inhibitors available, including neutralizing anti-VEGF antibodies such as bevacizumab (Avastin) and sorafenib (Nexavar). Sorafenib is a small molecular-weight (SMW) compound inhibiting multiple tyrosine kinases, including VEGF receptor (VEGFR) 2.[9]

The roles of pericytes in neoangiogenesis have also been well investigated.[10] Coverage of the neovasculature by pericytes stabilizes vascular structure.[11] Genetic ablation of platelet-derived growth factor (PDGF)-B signaling, one of the major signaling pathways in induction of pericyte maturation and recruitment to the endothelium, results in a bleeding tendency of the neovasculature.[11–13] PDGF-B signaling can be inhibited by the SMW inhibitor (SMWI) imatinib (Gleevec or Glivec), which inhibits the receptor for PDGF-B signaling, PDGF receptor (PDGFR) β, as well as PDGFRα and c-kit.[14] The use of imatinib along with VEGF inhibitors was shown to be effective in inhibiting tumor neovascularization in an animal model of spontaneous pancreatic islet tumor, the RIP-Tag model, through disruption of both pericytes and endothelium.[15]

Here we investigated the changes in vascular leakiness induced by three of the SMWI mentioned above, TGF-β inhibitor (LY364947), sorafenib, and imatinib, in the Matrigel plug assay as well as two animal cancer models. The Matrigel plug assay was carried out by mixing BD Matrigel Basement Membrane Matrix with VEGF-A, fibroblast growth factor (FGF)-2, and

[6]To whom correspondence should be addressed. E-mail: miyazono-ind@umin.ac.jp

doi: 10.1111/j.1349-7006.2008.01003.x

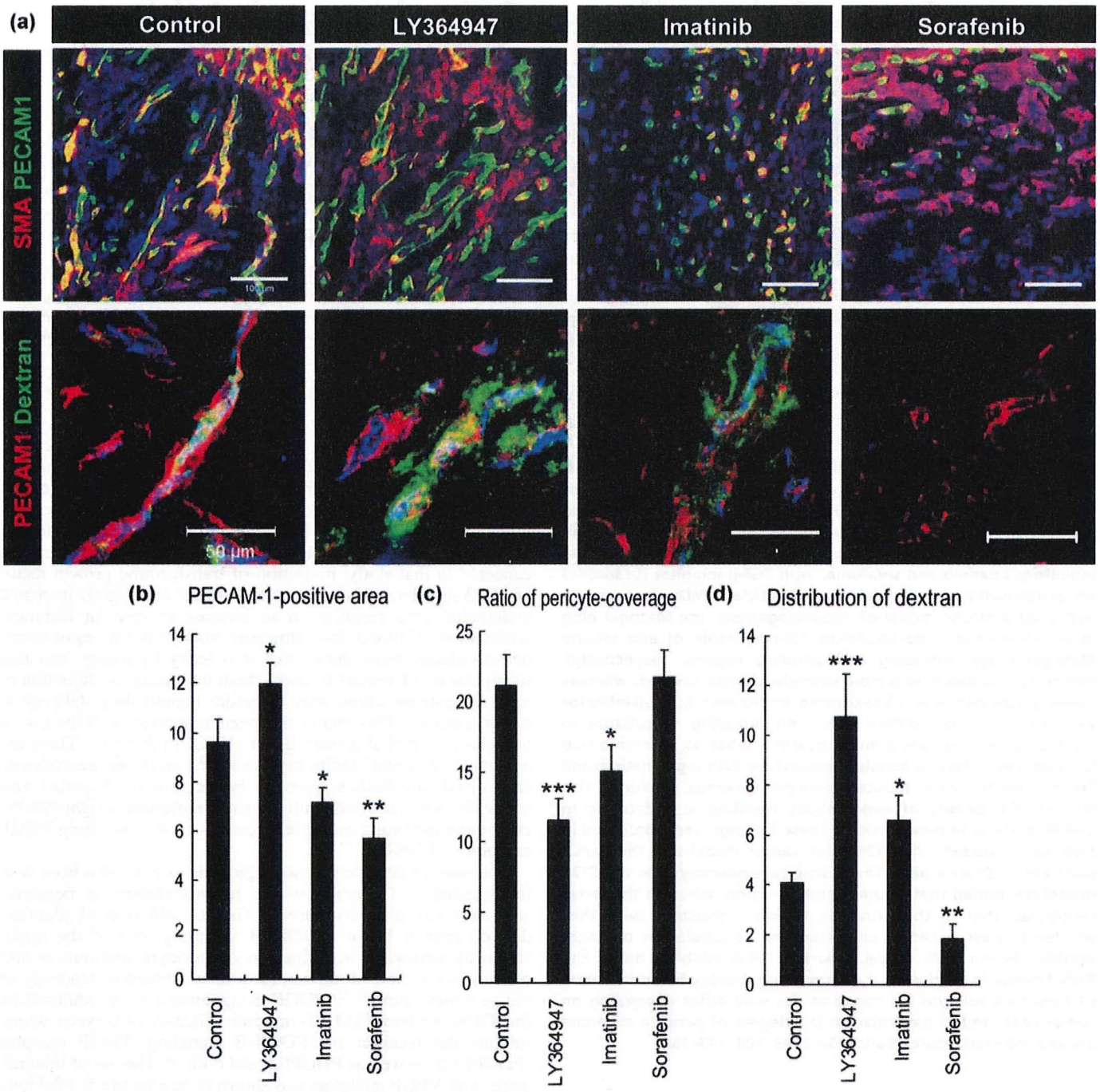

Fig. 1. The effects of three types of kinase inhibitors on extravasation of dextran in the Matrigel plug assay. (a) Confocal microscopy analyses. Upper row: staining of platelet endothelial cell adhesion molecule (PECAM)-1-positive endothelium in green and smooth muscle α-actin (SMA)-positive pericytes in red. Scale bars = 100 μm. Lower row: distribution of 2 MDa dextran in green and PECAM-1-positive endothelium in red. Scale bars = 50 μm. (b–d) Results of quantification (n = 15) of areas of endothelium (b, in percentage in one microscopic view), ratio of pericyte-covered endothelium (c, in percentage), and dextran distribution (d, in percentage in one microscopic view). Bars in the graphs represent standard errors. $^{*}P < 0.05$; $^{**}P < 0.01$; and $^{***}P < 0.001$.

heparin as angiogenic molecules to form mature neovasculature inside the gel plug, according to our previous report.[16] Of the two cancer models used in the present study, one was a well-established hypervascular cancer model using the murine colon cancer cell line CT26, whereas the other was an interstitium-rich cancer model using the human pancreatic cancer cell line BxPC3. With the latter model, we previously demonstrated therapeutic effects of combined use of TGF-β inhibitor on nanoparticles.[7] Using these models, we investigated the effects of SMWI on the distribution of 2 MDa dextran, a model of nanoparticles with an estimated hydrodynamic diameter of 50 nm.[6] The Matrigel plug assay and tumor model experiments revealed that TGF-β inhibitor increased extravasation of 2 MDa dextran in pericyte-covered neovasculature, whereas sorafenib increased that in vasculature with less pericyte coverage. These findings are important for determination of the optimal choice of angiogenic

doi: 10.1111/j.1349-7006.2008.01003.x

regulators in combination with nanoparticles for chemotherapy of cancer in general.

Materials and Methods

Reagents and antibodies. TGF-β inhibitor was purchased from Calbiochem (San Diego, CA, USA; LY364947, catalog no. 616451), imatinib was from Novartis Pharma (Tokyo, Japan), and sorafenib was from Bayer Healthcare (West Haven, CT, USA). These compounds were diluted in dimethyl sulfoxide to 5, 25, and 10 mg/mL, respectively, as stock solutions. Fluorescein isothiocyanate (FITC)-conjugated dextran of 2 000 000 Da (2 MDa) was obtained from Sigma-Aldrich (St Louis, MO, USA). The antibody to platelet endothelial cell adhesion molecule (PECAM)-1 was from BD PharMingen (San Diego, CA, USA), that to NG2 was from Chemicon (Temecula, CA, USA), and that to smooth muscle α-actin (SMA) (Cy3-conjugated) was from Sigma-Aldrich. AlexaFluor-conjugated secondary antibodies were purchased from Invitrogen Molecular Probes (Eugene, OR, USA).

Cancer cell lines and animals. The BxPC3 human pancreatic adenocarcinoma cell line was obtained from the American Type Culture Collection (Manassas, VA, USA), and was grown in RPMI-1640 medium supplemented with 10% fetal bovine serum. The murine colon adenocarcinoma CT26 cell line was from the National Cancer Center Research Institute, Japan, and was cultured in Dulbecco's modified Eagle's medium (Sigma-Aldrich) containing 10% fetal bovine serum. BALB/c mice and BALB/c nude mice, 5–6 weeks of age, were obtained from Sankyo Laboratory (Tokyo, Japan) and Charles River Laboratories (Tokyo, Japan), respectively.

***In vivo* Matrigel plug assay and cancer models.** Matrigel plugs were created by mixing 0.2 mg/mL recombinant human VEGF-A (VEGF165; R & D Systems, Minneapolis, MN, USA), 1 mg/mL FGF-2 (R & D Systems), and 0.1 mg/mL heparin (Aventis Pharma, Tokyo, Japan) by pipetting, in combination with regular Matrigel (catalogue no. 354234; BD Biosciences, Franklin Lakes, NJ, USA). Matrigel (400 μL per plug; one plug per mouse) was injected subcutaneously into the abdominal region of BALB/c mice. Each Matrigel plug was harvested on day 7 and frozen directly in dry-iced acetone for immunohistochemistry. As cancer models, 5×10^6 BxPC3 cells or 1×10^6 CT26 cells were implanted by subcutaneous injection into the abdominal region of BALB/c nude and normal BALB/c mice and allowed to grow for 3 weeks and 1 week, respectively, until reaching the proliferative phase. For the *in vivo* permeability assay, TGF-β inhibitor at 1 mg/kg, imatinib at 50 mg/kg, or sorafenib at 40 mg/kg was administered as one shot intraperitoneally 18 h before injection of dextran. Dextran was administered intravenously via lateral tail veins 6 h before harvesting of samples. For perfusion study in the tumor tissues, dextran of 2 MDa was administered intravenously, at 24 h after SMWI-administration and 10 min before harvesting, and the excised samples were directly fixed in formalin. All experimental protocols were carried out in accordance with the policies of the Animal Ethics Committee at the University of Tokyo.

Histology and immunohistochemistry. The excised samples were either directly frozen in dry-iced acetone for immunohistochemistry, or fixed overnight in 4% paraformaldehyde and then paraffin embedded to prepare them for hematoxylin–eosin (HE) staining or perfusion study in the tumor tissues. Frozen samples were further sectioned at 10 μm thickness in a cryostat, briefly fixed with 10% formalin, and then incubated with primary and fluorescent secondary antibodies. Samples were observed with a LSM510 Meta confocal microscope (Zeiss, Thornwood, NY, USA) for immunohistochemistry, and with an AX80 microscope (Olympus, Tokyo, Japan) for HE staining.

Quantification. Areas in Matrigel plugs that were PECAM-1-positive, double-positive for PECAM-1 and SMA, and FITC–dextran-positive in confocal micrographs ($n = 15$), or lengths of FITC–dextran-positive structure in the tumor tissues ($n = 12$) were measured using Adobe Photoshop software (Adobe Systems, San Jose, CA, USA) and ImageJ software (freeware distributed by the National Institutes of Health, USA). Pericyte coverage was quantified as the ratio of PECAM-1/SMA-double-positive areas to PECAM-1-positive areas, as described previously.[7] Results were further analyzed statistically by Student's *t*-test using Microsoft Excel software (Microsoft, Redmond WA, USA).

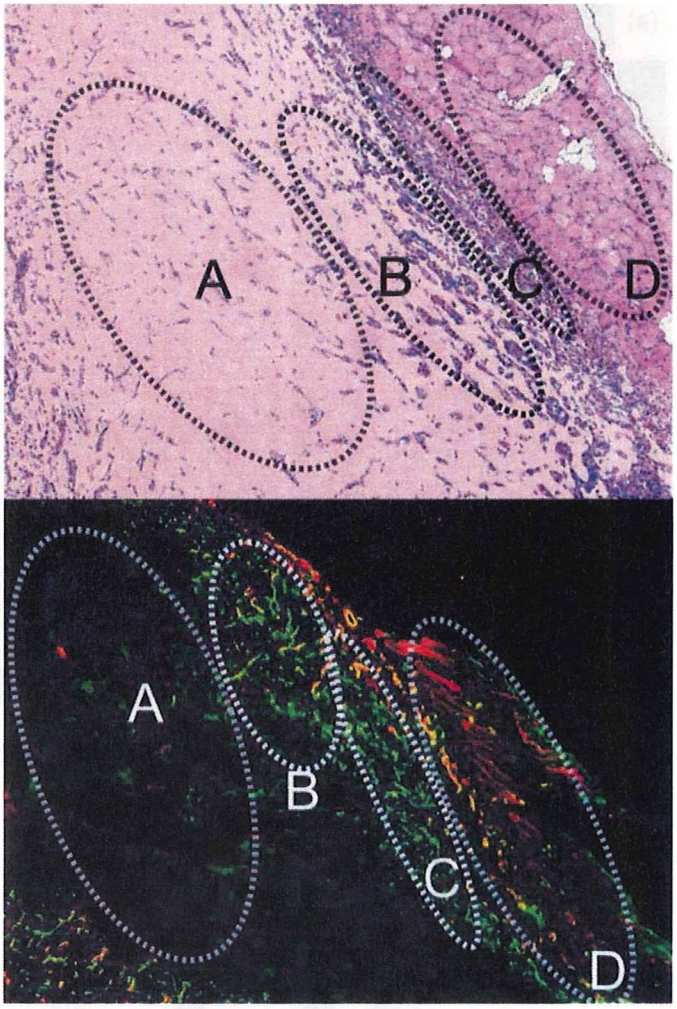

Fig. 2. Low-magnification view of the Matrigel plug and surrounding regions in sections with hematoxyline-eosin (HE) staining (upper) and with immunohistochemistry (lower). (a) Avascular area, (b) vascularized intraplug region, (c) periplug region, and (d) normal tissue. Green, platelet endothelial cell adhesion molecule-1; red, smooth muscle α-actin.

Results

We initially carried out the Matrigel plug assay *in vivo*, in which regular Matrigel was mixed with VEGF-A, FGF-2, and heparin[16] to investigate the effects of three SMWI on the extravasation of 2 MDa dextran (Fig. 1). Marked induction of pericyte-covered mature neovasculature was observed in the gel plug after a 7-day incubation in mice, as we reported previously.[16] Pericytes were determined to be SMA-positive cells in a Matrigel plug assay. In this model, administration of TGF-β inhibitor decreased pericyte coverage of the neovasculature and significantly enhanced the distribution of 2 MDa dextran. This observation was consistent

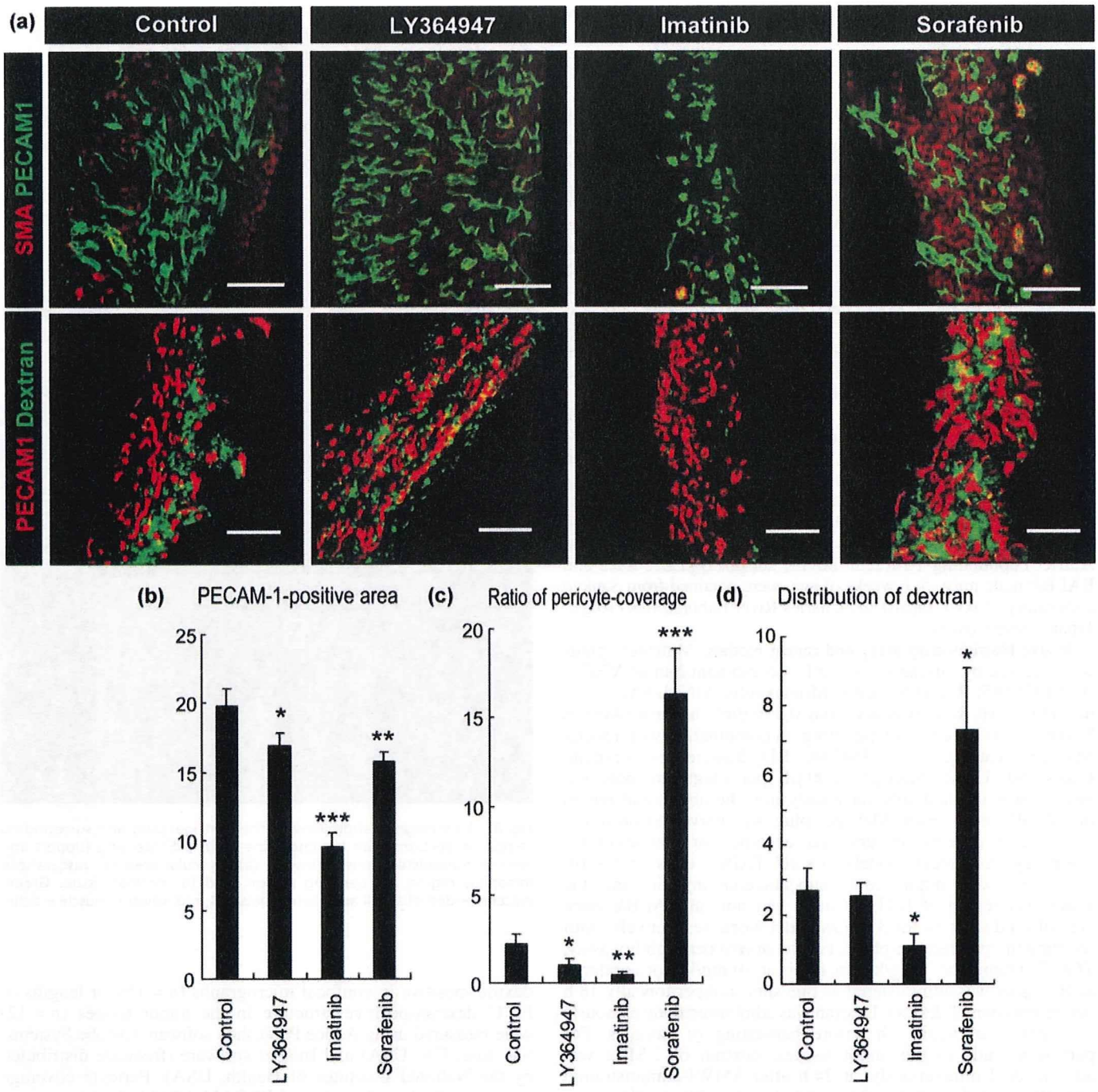

Fig. 3. Effects of three types of kinase inhibitors on extravasation of dextran from vasculature in the periplug region. (a) Confocal microscopy analyses. Upper row: staining of platelet endothelial cell adhesion molecule (PECAM)-1-positive endothelium in green and smooth muscle α-actin (SMA)-positive pericytes in red. Lower row: distribution of 2 MDa dextran in green and PECAM-1-positive endothelium in red. Scale bars = 100 μm. (b–d) Results of quantification (n = 15) of areas of endothelium (b, in percentage in one microscopic view), ratio of pericyte-covered endothelium (c, in percentage), and dextran distribution (d, in percentage in one microscopic view). Bars in the graphs represent standard errors. $^{*}P < 0.05$; $^{**}P < 0.01$; and $^{***}P < 0.001$.

with our previous study, in which we used animal models of pancreatic adenocarcinoma and diffuse-type gastric cancer.[7] Based on this result, we expected that a decrease in pericytes might induce more extravasation of 2 MDa dextran.

To confirm this, we compared the effects of imatinib administration, which inhibits PDGF signaling and may therefore decrease pericyte coverage. However, administration of imatinib decreased the total accumulation of 2 MDa dextran compared with TGF-β inhibitor (Fig. 1). Although imatinib actually decreased pericyte coverage to the same level of TGF-β inhibitor, it also decreased PECAM-1-positive endothelium together with pericyte coverage. These findings of morphological analysis were consistent with those noted in a previous report.[17] TGF-β inhibitor maintained the area of PECAM-1-positive endothelium and may therefore be superior to imatinib. In addition, although VEGF inhibition was expected to increase drug delivery, based on the

doi: 10.1111/j.1349-7006.2008.01003.x

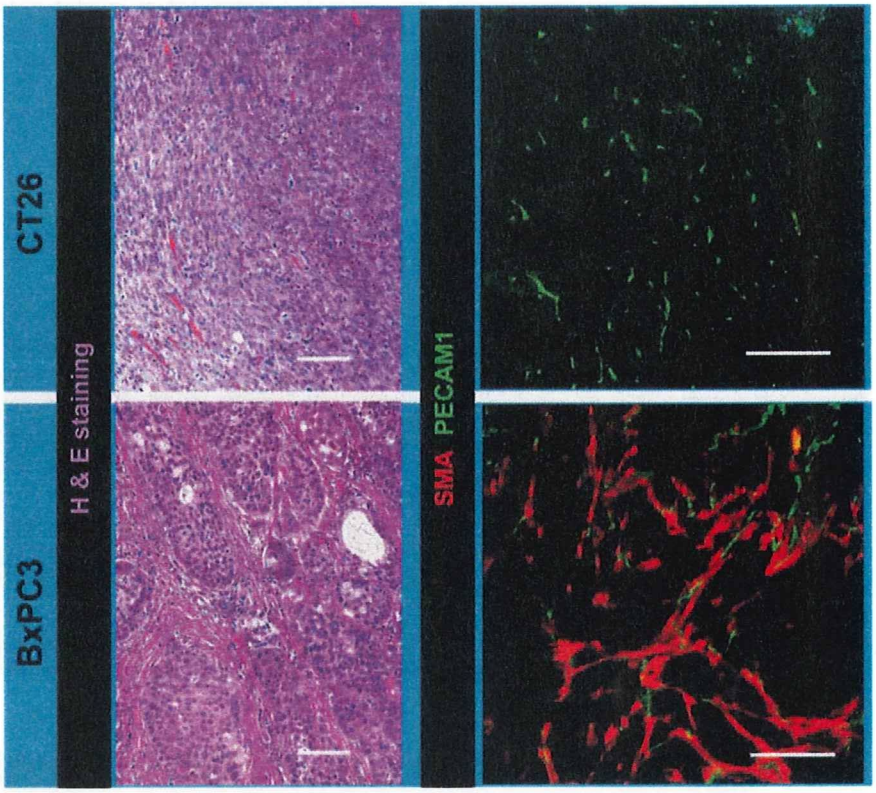

Fig. 4. Two animal tumor models using CT26 and BxPC3 cell lines. Histological examination of tumor models by hematoxylin–eosin staining and immunohistochemistry with platelet endothelial cell adhesion molecule (PECAM)-1 in green and smooth muscle α-actin (SMA) in red. Scale bars = 100 μm.

results of previous studies,[8] sorafenib nearly eliminated the influx of 2 MDa dextran and resulted in far less accumulation of it. This result can be explained by the potent reduction of PECAM-1-positive endothelium and increase in pericytes as sleeves. These morphological changes induced by VEGF inhibition were also consistent with previous reports.[18]

Although the neovasculature inside the gel plugs was as described above, the vasculature in the regions surrounding the gel plugs, or sites of acute inflammation in reaction to the plugs as foreign bodies (Fig. 2), exhibited different patterns. Compared to the vasculature inside the gel plug, that in regions around the plugs was denser and more tortuous, and was accompanied by pericytes to a smaller extent. These phenotypes resembled those of the vasculature in conventional animal models of tumors, such as the CT26 model, as we describe later in this report. We termed these two regions the 'intraplug' and 'periplug' regions, respectively, after the established terminology in oncology, 'intratumoral' and 'peritumoral'.

Functionally, the vasculature in periplug regions was leaky to 2 MDa dextran in the control condition, that is, without any modulation by SMWI (Fig. 3). Surprisingly, the effects of SMWI on neovasculature in the periplug regions were quite different from those in the intraplug regions. In the periplug regions, pericyte coverage of the neovasculature was far less than in the intraplug region, even in the control condition. In this periplug region, neither TGF-β inhibitor nor imatinib significantly altered pericyte coverage. Consequently, these compounds did not alter the accumulation of 2 MDa dextran. Sorafenib, on the other hand, did increase pericyte coverage, and increased the accumulation of 2 MDa dextran. This increase in extravasation was consistent with previous reports on the effects of VEGF inhibition.[8]

We subsequently compared these findings in the Matrigel plug assay with those in two subcutaneous tumor xenograft models. We used the CT26 cell line derived from murine colon cancer and the BxPC3 cell line derived from human pancreatic adenocarcinoma (Fig. 4). HE staining of CT26 xenografts revealed a well-vascularized medullary histological pattern with little tumor stroma, whereas that of BxPC3 xenografts revealed a stroma-rich histology. Immunostaining of PECAM-1 and SMA confirmed this stroma-rich characteristic of the BxPC3 model. Although the BxPC3 model grew more slowly than the CT26 model, the BxPC3 model also reached the proliferative phase. Compared to the BxPC3 model, the CT26 model required one-fifth of the number of inoculating cells and one-third of the duration to reach the proliferative phase, which was 1 week for the CT26 model and 3 weeks for the BxPC3 model (data not shown). These differences may well be due to the differences in requirements for induction of stromal components from host animals, as well as rates of proliferation of tumor cell lines.

We then tested the alterations in vascular phenotypes as well as accumulation of 2 MDa dextran with or without SMWI in these tumor models (Fig. 5). We here used NG2 as the pericyte marker (Fig. 5a), because SMA-positive cells (i.e. myofibroblasts) are abundant especially in the stroma of BxPC3 tumor (Fig. 4). In the CT26 model, sorafenib did increase the pericyte-covered vasculature, whereas other SMWI did not increase the pericytes. Imatinib decreased endothelial cells. These observations in the CT26 tumor model were consistent with those in the periplug region of the Matrigel plug. In the BxPC3 model, pericyte coverage was less with LY364947 and imatinib, and endothelial cells were decreased with imatinib and sorafenib. These findings in the BxPC3 tumor model were consistent with those in the intraplug region. Accordingly, 2 MDa dextran was diffusely distributed in tumor tissue without any treatment in the CT26 model, whereas almost no leakage of dextran was observed in the BxPC3 model (Fig. 5b). Sorafenib exhibited the best effect in the CT26 model, whereas TGF-β inhibitor did in the BxPC3 model. The latter result was consistent with the findings of our previous work using nanoparticles including PEGylated liposomes incorporating doxorubicin (Doxil) of approximately 100 nm in diameter, which exhibited antitumor effects in the BxPC3 model

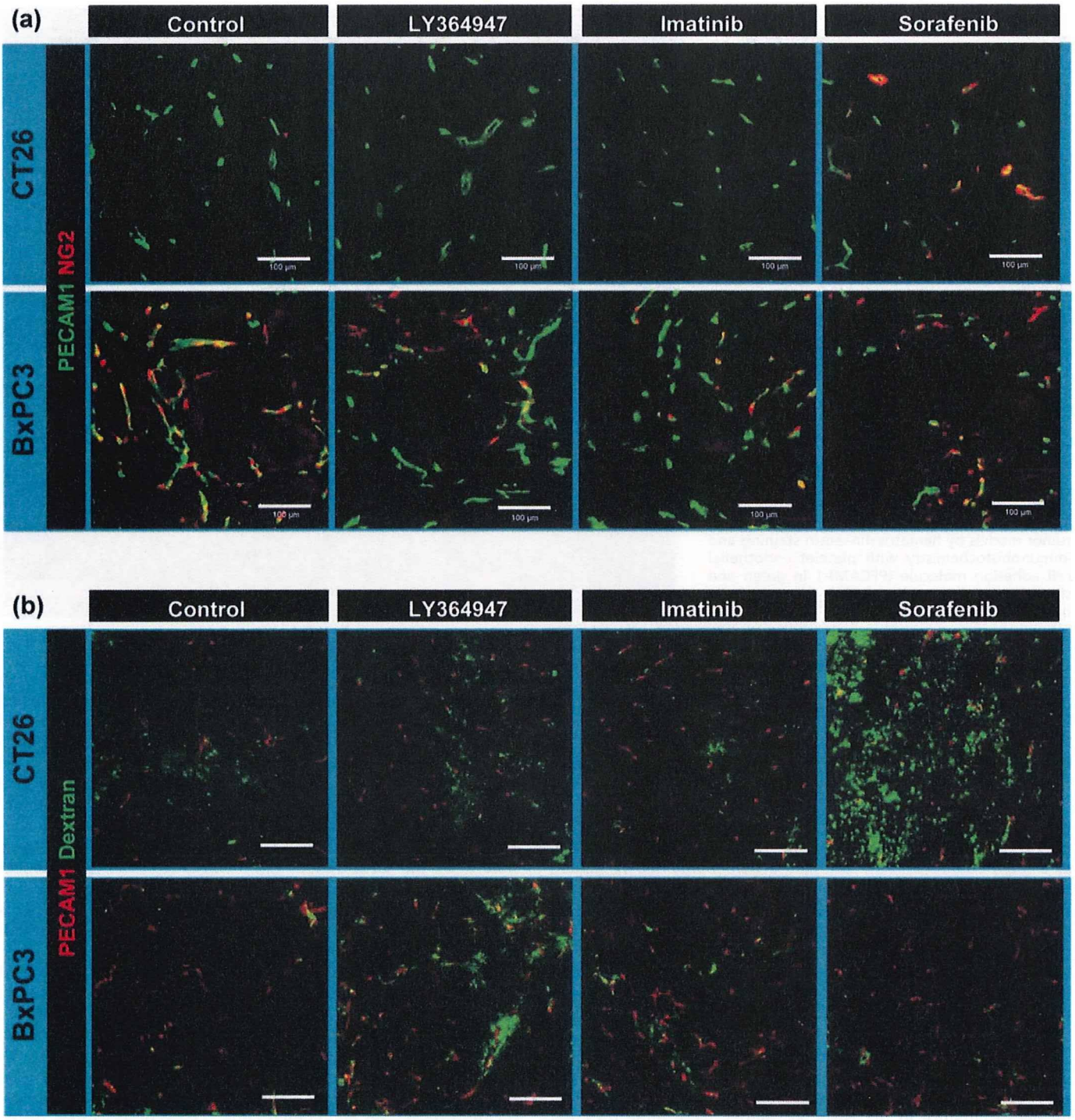

Fig. 5. Effects of three kinase inhibitors in the tumor models. (a) Vascular phenotypes revealed by immunohistochemistry. Green, platelet endothelial cell adhesion molecule (PECAM)-1; red, NG2. (b) Extravasation of 2 MDa dextran from vasculature. Dextran in green and PECAM-1 in red. Scale bars = 100 μm.

only when combined with TGF-β inhibitor.[7] We also tested the effects of Doxil with or without TGF-β inhibitor in the CT26 model. Monotherapy with Doxil at 8 mg/kg almost completely inhibited tumor growth, and combined administration of TGF-β inhibitor did not yield any significant additional effects (data not shown). These findings were consistent with those observed in the Matrigel plug assay. The effects of combined use of imatinib were also consistent with those in the Matrigel plug assay.

Increased accumulation of dextran in these tumor models at 7 h after injection, by sorafenib in the CT26 tumor and by LY364947 in the BxPC3 tumor, can also be explained by an increase in the amount of vasculature with perfusion, not only by an increase in leakage. To test this possibility, we examined changes in perfusion by intravascular existence of dextran at only 10 min after administration, because dextran of 2 MDa should basically remain inside vasculature at that time after

doi: 10.1111/j.1349-7006.2008.01003.x

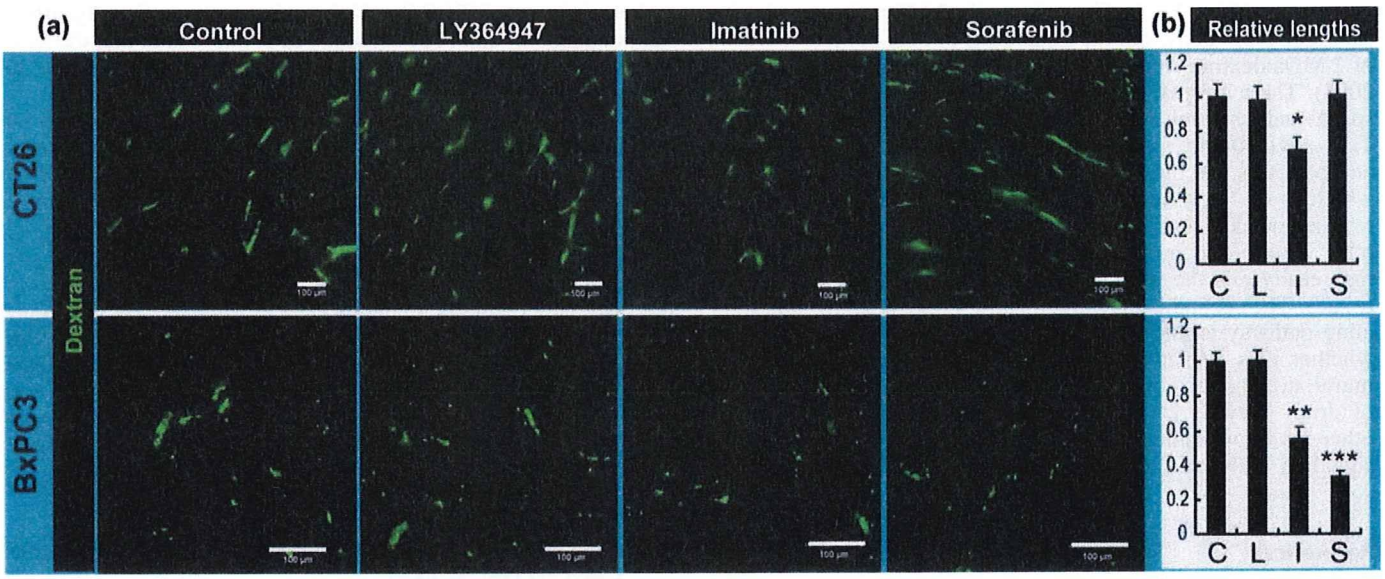

Fig. 6. Perfusion study in the tumor models. (a) Tumor vessels with perfusion were determined by the existence of dextran in green, administrated at 10 min before harvesting. Scale bars = 100 μm. (b) Relative lengths of vessels with perfusion. C, control; I, imatinib; L, LY364947; S, sorafenib. Bars represent standard errors. $*P < 0.05$; $**P < 0.01$; and $***P < 0.001$.

injection.[6] As shown in Figure 6, the lengths of vasculature with blood flow were not altered in the conditions exhibiting increased accumulation of dextran, that is, by sorafenib treatment in the CT26 tumor and by LY364947 treatment in the BxPC3 tumor. Therefore, the increased accumulation of dextran in these conditions may largely be due to an increase in vascular leakiness.

Discussion

We have previously shown that use of short-acting SMW TGF-β inhibitor can increase the distribution of nanoparticles in stroma-rich tumors by increasing the leakiness of the tumor neovasculature.[7] By virtue of the brief duration of SMWI effects, potential side effects can be decreased due to long-term suppression of essential signaling pathways. There are still a number of SMWI that can be used for manipulation of tumor neovasculature via their effects on pericytes or endothelium. We therefore compared the effects of two of these SMWI, imatinib and sorafenib.

Combined use of VEGF inhibition has been reported to have potent effects on drug delivery into tumor tissues.[19] The underlying mechanism for this has been explained by the vascular 'normalization' theory,[8] or decreased interstitial fluid pressure by decreased leakiness of tumor vasculature, via a decrease in endothelial cells and increase in pericyte coverage. Consistent with this, VEGF inhibition by sorafenib had significant effects on the retention of 2 MDa dextran in the periplug regions and in CT26 tumor, where vasculature showed less pericyte coverage and denser endothelium than in normal tissues. However, VEGF inhibition significantly decreased retention of the same dextran in adjacent areas, the intraplug region, and in BxPC3 tumor. Vascular phenotypes in these regions were characterized by more pericyte coverage and sparser endothelium, that is, they were more 'normal' than those in the periplug region and in CT26 tumor.

One of the differences between these two kinds of vasculature was the blood flow in the vasculature after sorafenib treatment. In CT26 tumor after sorafenib treatment, blood flow was maintained, whereas the flow ceased in sorafenib-treated BxPC3 tumor. These differences may partially be because of differences in sensitivity of the endothelium to the change in VEGF signaling, known to be at least due to differences in expression levels of VEGFR2.[18]

Another apparent difference in these tumor models was pericyte coverage before drug administration. Less pericyte coverage has been reported to result in more leakiness.[11–13] The degrees of dextran accumulation in all control conditions (i.e. without modification by SMWI) are consistent with the degrees of pericyte coverage. Increased dextran accumulation in LY364947-treated BxPC3 tumors can also be explained by decreased pericyte coverage, not by normalization. Both blood perfusion (Fig. 6) and interstitial fluid pressure, which we previously reported,[7] did not differ with or without LY364947 treatment in BxPC3 tumor. These findings suggest that we may need different approaches, such as the use of TGF-β inhibitor to increase drug delivery (at least for nanoparticles), to develop effective treatment for tumors with originally 'more normal' tumor vasculature. Note, however, that these more normal vessels in tumors might not be completely normal, because TGF-β inhibitor did not alter the accumulation of nanoparticles in true normal tissues, as we previously reported.[7]

Regarding the degree of original pericyte coverage in tumor vasculature, an increase in the amount of stromal components in tumor tissue may result in an increase in pericyte coverage. In a previous study, we found that the presence of FGF-2 together with VEGF-A enhances mature neovascularization compared with VEGF-A alone.[16] In addition to FGF-2, a set of signaling molecules is needed to recruit and to induce proliferation of pericytes. These include PDGF-BB[12,13] (homodimer of PDGF-B chain) and TGF-β.[11,20] These signaling molecules are reported to be secreted from components of the tumor stroma and, above all, cancer-associated fibro-blasts[21–23] and macrophages.[24] Tumors with more stroma, including fibroblasts and immune cells, have more pericyte coverage of the vasculature with greater maturity and less leakiness. Although chemoresistance of tumors has been largely investigated from the aspect of drug sensitivity of tumor cells per se, it is possible that the histological pattern of the tumor tissues may also constitute a reason for chemoresistance, because of insufficient drug delivery to the tumor cells.

The Tie2–angiopoietin signaling pathway is also known to be involved in vessel maturation and to affect pericytes.[25] Because there are no SMW compounds available to inhibit this signaling pathway, we tested the effects of one-shot Tie2-Fc chimeric

protein at 50 mg/kg bodyweight with 2 MDa dextran in the Matrigel plug assay, but no significant effects on accumulation of 2 MDa dextran were observed (M.R. Kano, unpublished data, 2008). There are two possible explanations for this observation: spatial and temporal. According to the spatial explanation, because Tie2–angiopoietin signaling occurs between the endothelium and pericytes and thus outside the vessel lumen, the Fc chimera, which is of fairly large molecular size and may therefore be retained inside vessel lumens, is not able to affect signaling. The other drugs used in the present study were all SMWI, which may easily exit the vessel lumen and penetrate the perivascular tissues. The second explanation is temporal. Although this signaling pathway is known to be deeply involved in development, whether it is also involved in the maintenance of endothelial-mural structure is not known. Because we observed the effects of drugs only at 24 h after administration, it is possible that other inhibitors inhibited only the maintenance functions of the signaling pathways, and not functions related to development. Administration of TGF-β inhibitor did not significantly affect the vasculature in normal organs,[7] so it is possible that the neovasculature requires larger amounts of signaling molecules to maintain structure than do established vessels.

In conclusion, the appropriate strategy for optimization of tumor vasculature for drug delivery system using nanoparticles may not be uniform, and may depend on tumor type, including differences in the degree of pericyte coverage of tumor vasculature.

Acknowledgments

We thank Dr Peter Baluk, Cardiovascular Research Institute, University of California, San Francisco (UCSF), for advice about perfusion. This work was supported by Grant-in-Aid for Scientific Research (KAKENHI 19790282 and 17016011) from the Ministry of Education, Culture, Sports, and Technology of Japan (MEXT), and a Health Labor Sciences Research Grant from the Ministry of Health, Labor, and Welfare of Japan.

References

1 Giroux V, Malicet C, Barthet M *et al.* p8 is a new target of gemcitabine in pancreatic cancer cells. *Clin Cancer Res* 2006; **12**: 235–41.
2 Merriman RL, Hertel LW, Schultz RM *et al.* Comparison of the antitumor activity of gemcitabine and ara-C in a panel of human breast, colon, lung and pancreatic xenograft models. *Invest New Drugs* 1996; **14**: 243–7.
3 Rothenberg ML, Moore MJ, Cripps MC *et al.* A phase II trial of gemcitabine in patients with 5-FU-refractory pancreas cancer. *Ann Oncol* 1996; **7**: 347–53.
4 Hanahan D, Weinberg RA. The hallmarks of cancer. *Cell* 2000; **100**: 57–70.
5 Jain RK. Physiological barriers to delivery of monoclonal antibodies and other macromolecules in tumors. *Cancer Res* 1990; **50**: 814S–19S.
6 Dreher MR, Liu W, Michelich CR, Dewhirst MW, Yuan F, Chilkoti A. Tumor vascular permeability, accumulation, and penetration of macromolecular drug carriers. *J Natl Cancer Inst* 2006; **98**: 335–44.
7 Kano MR, Bae Y, Iwata C *et al.* Improvement of cancer-targeting therapy, using nanocarriers for intractable solid tumors by inhibition of TGF-β signaling. *Proc Natl Acad Sci USA* 2007; **104**: 3460–5.
8 Jain RK. Normalization of tumor vasculature: an emerging concept in antiangiogenic therapy. *Science* 2005; **307**: 58–62.
9 Wilhelm S, Carter C, Lynch M *et al.* Discovery and development of sorafenib: a multikinase inhibitor for treating cancer. *Nat Rev Drug Discov* 2006; **5**: 835–44.
10 Bergers G, Song S. The role of pericytes in blood-vessel formation and maintenance. *Neuro Oncol* 2005; **7**: 452–64.
11 von Tell D, Armulik A, Betsholtz C. Pericytes and vascular stability. *Exp Cell Res* 2006; **312**: 623–9.
12 Abramsson A, Lindblom P, Betsholtz C. Endothelial and nonendothelial sources of PDGF-B regulate pericyte recruitment and influence vascular pattern formation in tumors. *J Clin Invest* 2003; **112**: 1142–51.
13 Lindblom P, Gerhardt H, Liebner S *et al.* Endothelial PDGF-B retention is required for proper investment of pericytes in the microvessel wall. *Genes Dev* 2003; **17**: 1835–40.
14 Buchdunger E, Zimmermann J, Mett H *et al.* Inhibition of the Abl protein-tyrosine kinase *in vitro* and *in vivo* by a 2-phenylaminopyrimidine derivative. *Cancer Res* 1996; **56**: 100–4.
15 Bergers G, Song S, Meyer-Morse N, Bergsland E, Hanahan D. Benefits of targeting both pericytes and endothelial cells in the tumor vasculature with kinase inhibitors. *J Clin Invest* 2003; **111**: 1287–95.
16 Kano MR, Morishita Y, Iwata C *et al.* VEGF-A and FGF-2 synergistically promote neoangiogenesis through enhancement of endogenous PDGF-B–PDGFRβ signaling. *J Cell Sci* 2005; **118**: 3759–68.
17 Vlahovic G, Rabbani ZN, Herndon JE, Dewhirst MW, Vujaskovic Z. Treatment with Imatinib in NSCLC is associated with decrease of phosphorylated PDGFR-β and VEGF expression, decrease in interstitial fluid pressure and improvement of oxygenation. *Br J Cancer* 2006; **95**: 1013–19.
18 Mancuso MR, Davis R, Norberg SM *et al.* Rapid vascular regrowth in tumors after reversal of VEGF inhibition. *J Clin Invest* 2006; **116**: 2610–21.
19 Hurwitz H, Fehrenbacher L, Novotny W *et al.* Bevacizumab plus irinotecan, fluorouracil, and leucovorin for metastatic colorectal cancer. *N Engl J Med* 2004; **350**: 2335–42.
20 Hirschi KK, Rohovsky SA, D'Amore PA. PDGF, TGF-β, and heterotypic cell–cell interactions mediate endothelial cell-induced recruitment of 10T1/2 cells and their differentiation to a smooth muscle fate. *J Cell Biol* 1998; **141**: 805–14.
21 Pietras K, Pahler J, Bergers G, Hanahan D. Functions of paracrine PDGF signaling in the proangiogenic tumor stroma revealed by pharmacological targeting. *PLoS Med* 2008; **5**: e19.
22 Micke P, Ostman A. Tumour–stroma interaction: cancer-associated fibroblasts as novel targets in anti-cancer therapy? *Lung Cancer* 2004; **45**: S163–75.
23 Bhowmick NA, Moses HL. Tumor–stroma interactions. *Curr Opin Genet Dev* 2005; **15**: 97–101.
24 Lewis CE, Pollard JW. Distinct role of macrophages in different tumor microenvironments. *Cancer Res* 2006; **66**: 605–12.
25 Armulik A, Abramsson A, Betsholtz C. Endothelial/pericyte interactions. *Circ Res* 2005; **97**: 512–23.

doi: 10.1111/j.1349-7006.2008.01003.x

Pharmaceutical Research, Vol. 25, No. 12, December 2008 (© 2008)
DOI: 10.1007/s11095-008-9720-2

Research Paper

Polyplex Micelles from Triblock Copolymers Composed of Tandemly Aligned Segments with Biocompatible, Endosomal Escaping, and DNA-Condensing Functions for Systemic Gene Delivery to Pancreatic Tumor Tissue

Kanjiro Miyata,[1,6] Makoto Oba,[2] Mitsunobu R. Kano,[3,6] Shigeto Fukushima,[4] Yelena Vachutinsky,[1] Muri Han,[5] Hiroyuki Koyama,[2] Kohei Miyazono,[3,6] Nobuhiro Nishiyama,[4,6] and Kazunori Kataoka[1,4,5,6,7]

Received June 26, 2008; accepted August 26, 2008; published online September 10, 2008

Purpose. For systemic gene delivery to pancreatic tumor tissues, we prepared a three-layered polyplex micelle equipped with biocompatibility, efficient endosomal escape, and pDNA condensation functions from three components tandemly aligned; poly(ethylene glycol) (PEG), a poly(aspartamide) derivative with a 1,2-diaminoethane moiety (PAsp(DET)), and poly(L-lysine).
Materials and Methods. The size and *in vitro* transfection efficacy of the polyplex micelles were determined by dynamic light scattering (DLS) and luciferase assay, respectively. The systemic gene delivery with the polyplex micelles was evaluated from enhanced green fluorescence protein (EGFP) expression in the tumor tissues.
Results. The polyplex micelles were approximately 80 nm in size and had one order of magnitude higher *in vitro* transfection efficacy than that of a diblock copolymer as a control. With the aid of transforming growth factor (TGF)-β type I receptor (TβR-1) inhibitor, which enhances accumulation of macromolecular drugs in tumor tissues, the polyplex micelle from the triblock copolymer showed significant EGFP expression in the pancreatic tumor (BxPC3) tissues, mainly in the stromal regions including the vascular endothelial cells and fibroblasts.
Conclusion. The three-layered polyplex micelles were confirmed to be an effective gene delivery system to subcutaneously implanted pancreatic tumor tissues through systemic administration.

KEY WORDS: gene delivery; PEG; polyplex micelle; TGF-β inhibitor; triblock copolymer.

INTRODUCTION

Successful gene delivery through systemic administration is crucial for the gene therapy of various intractable diseases, including cancer. Use of an appropriate gene vector is needed for systemic administration to achieve selective accumulation of the intact gene in target tissues, and subsequently, to reveal effective gene expression with a sufficient therapeutic index. Although major gene vectors in clinical trials are viral-based systems (1), they could have risks of immunogenicity and mutagenicity that would interfere with their practical use in clinics. Synthetic polymer-based vectors (polyplexes) are attractive alternatives of viruses, because of much lower immunogenicity, greater ease of chemical modification and larger-scale preparation (2–4). To attain successful transfection in tumor tissues *via* intravenous administration by polyplex vectors, several important issues as follows should be addressed: (1) high stability to protect the DNA structure in the biological milieu from nuclease attack, (2) minimized non-specific interaction with biological components to exert longevity in the blood circulation, and (3) smooth escape from endosomes to cytoplasm for efficient gene expression inside target cells.

To fulfill such requirements, polyplexes with poly(ethylene glycol) (PEG) palisades (polyplex micelle) have been prepared by several groups including ourselves through the self-assembly of PEG-polycation copolymers with plasmid DNA (pDNA) (4–8). Indeed, polyplex micelles prepared from PEG–poly(L-lysine) block copolymer (PEG–PLys) showed high tolerability in serum media (9), allowing for a prolonged circulation period of intact pDNA in the blood stream, whereas naked pDNA was completely digested within

[1] Department of Bioengineering, Graduate School of Engineering, The University of Tokyo, 7-3-1 Hongo, Bunkyo-ku, Tokyo, 113-8656, Japan.
[2] Department of Clinical Vascular Regeneration, Graduate School of Medicine, The University of Tokyo, 7-3-1 Hongo, Bunkyo-ku, Tokyo, 113-8655, Japan.
[3] Department of Molecular Pathology, Graduate School of Medicine, The University of Tokyo, 7-3-1 Hongo, Bunkyo-ku, Tokyo, 113-8655, Japan.
[4] The Center for Disease Biology and Integrative Medicine, Graduate School of Medicine, The University of Tokyo, 7-3-1 Hongo, Bunkyo-ku, Tokyo, 113-0033, Japan.
[5] Department of Materials Engineering, Graduate School of Engineering, 7-3-1 Hongo, Bunkyo-ku, Tokyo, 113-8656, Japan.
[6] Center for NanoBio Integration, The University of Tokyo, 7-3-1 Hongo, Bunkyo-ku, Tokyo, 113-8656, Japan.
[7] To whom correspondence should be addressed. (e-mail: kataoka@bmw.t.u-tokyo.ac.jp)

0724-8741/08/1200-2924/0

5 min (10). Nevertheless, PLys-based systems have encountered the issue of inefficient transfection activity, because of the lack of endosome escape, involving a "proton sponge effect" caused by amino groups with a low pKa value as typically reported in poly(ethylenimine) (PEI)-based systems (11,12). Worth noting in this regard is our recent finding that polyplexes from a poly(aspartamide) derivative having 1,2-diaminoethane unit as a side chain, poly{*N*-[*N*-(2-aminoethyl)-2-aminoethyl]aspartamide} (PAsp(DET)), revealed highly efficient transfection with minimal cytotoxicity to a variety of cells including primary cells (13–16), probably due to facilitated endosomal escape based on remarkable change in the protonation degree between physiological pH and endosomal acidic pH. Actually, the PEG–PAsp(DET) polyplex micelle succeeded in *in vivo* transfection of a reporter gene (luciferase) to a rabbit's clamped carotid artery *via* intra-arterial injection (17). Also, when the PEG–PAsp(DET) polyplex micelle was incorporated into a calcium phosphate cement scaffold and then applied in a bone defect model to a mouse skull bone, substantial bone formation surrounding the entire lower surface of the implant was induced by the regulated release of the micelles containing a constitutively active form of activin receptor-like kinase 6 (caALK6) and runt-related transcription factor 2 (Runx2) genes from the scaffold (18). The relatively weak affinity of PAsp(DET) segments to pDNA (19) is also an advantage for the smooth release of the incorporated pDNA and subsequent efficient transcription in the cell interior. On the other hand, such weak affinity probably leads to the detachment of PAsp (DET) chains from pDNA in the polyplex micelle through the interaction with biological components during circulation in the blood stream, resulting in a loss of transfection activity. Therefore, strategies to stabilize the structure of the polyplex micelles against PEG–PAsp(DET) are needed for the development of effective systemic administration methods.

The present study was devoted to develop a PEG–PAsp (DET)-based polyplex micelle for systemic use by conjugating a PLys segment as an anchoring moiety to pDNA at the ω-end of the diblock copolymer. For this purpose, a triblock copolymer of poly(ethylene glycol)-poly{*N*-[*N*-(2-aminoethyl)-2-aminoethyl]aspartamide}-poly(L-lysine) (PEG–PAsp (DET)–PLys) was prepared to integrate three functional segments engendering biocompatibility (PEG), efficient endosomal escape (PAsp(DET)), and effective pDNA condensation (PLys), respectively. In this way, three-layered polyplex micelles can be constructed, in which the middle layer, functioning as an endosomal escape element, is sandwiched between an outer layer of biocompatible PEG and an inner layer of PLys/pDNA polyplex (20). The fluorescence measurement with an intercalator into DNA indicated that pDNA mixed with the triblock copolymers was condensed more tightly than in a PEG–PAsp(DET) diblock copolymer and comparably to a PEG–PLys diblock copolymer. Intracellular trafficking of the polyplex micelles with or without the intermediate layer of PAsp(DET) was compared in detail by confocal fluorescence microscopy to reveal the endosomal escape of the micelles with the PAsp(DET) layer. Finally, reporter gene expression in a subcutaneous pancreatic tumor model, representing an intractable solid tumor with thick fibrosis and hypovascularity, demonstrated that the intravenously injected three-layered polyplex micelles effectively penetrated tumor vasculature in combination with transforming growth factor (TGF)-β type I receptor inhibitor (TβR-I) (21).

MATERIALS AND METHODS

Materials

α-Methoxy-ω-amino-poly(ethylene glycol) (Mw 12,000; PEG–NH_2) and β-benzyl-L-aspartate *N*-carboxy-anhydride (BLA–NCA) were obtained from Nippon Oil and Fats Co., Ltd. (Tokyo, Japan). ε-(Benzyloxycarbonyl)-L-lysine *N*-carboxy anhydride (Lys(Z))–NCA was synthesized from ε-(benzyloxycarbonyl)-L-lysine (Wako Pure Chemical Industries, Ltd., Osaka, Japan) by the Fuchs-Farthing method using bis(trichloromethyl) carbonate (triphosgene; Tokyo Kasei Kogyo Co., Ltd., Tokyo, Japan) (22). Diethylenetriamine (DET; bis(2-aminoethyl)amine), *N*,*N*-dimethylformamide (DMF), dichloromethane, benzene, trifluoroacetic acid, *N*-methyl 2-pyrrolidone (NMP), Tris (tris(hydroxymethyl) aminomethane) and HEPES (2-[4-(2-hydroxyethyl)-1-piperazinyl]ethanesulfonic acid) were purchased from Wako Pure Chemical Industries, Ltd., Osaka, Japan. DMF and dichloromethane distilled by conventional methods were used for the polymer synthesis. DET was distilled over CaH_2 under reduced pressure, and then used for the aminolysis reaction. A pDNA coding for luciferase with a CAG promoter provided by RIKEN (Japan) was used after the amplification in competent DH5α *Escherichia coli* and the subsequent purification using a HiSpeed Plasmid MaxiKit purchased from QIAGEN Science Co., Inc. (Germantown, MD, USA). A full-size Label IT Cy5 Labeling Kit was purchased from Mirus Bio Corporation (Madison, WI, USA). Twenty-four- and 96-well culture plates were purchased from Becton Dickinson Labware (Franklin Lakes, NJ, USA). A human hepatocyte, Huh-7, was obtained from the RIKEN Cell Bank (RIKEN Bioresource Center, Japan). A human pancreatic adenocarcinoma cell line, BxPC3, was obtained from the American Type Culture Collection (Manassas, VA, USA). Dulbecco's Modified Eagle's Medium (DMEM) and RPMI medium 1640 were purchased from Sigma-Aldrich Co. (St. Louis, MO, USA). Fetal bovine serum (FBS) was purchased from Dainippon Sumitomo Parma Co., Ltd. (Osaka, Japan). A Luciferase Assay System Kit was purchased from Promega Co. (Madison, WI, USA), and a Micro BCA™ Protein Assay Reagent Kit was purchased from Pierce Co., Inc. (Rockford, IL, USA). TβR-I inhibitor was purchased from Calbiochem (San Diego, CA, USA; LY364947; catalog no. 616451). Rat monoclonal antibody anti-platelet endothelial cell adhesion molecule-1 (PECAM-1), as a marker for vascular endothelial cells, was purchased from BD Pharmingen (Franklin Lakes, NJ, USA), and Alexa647-conjugated secondary antibody to rat IgG was from Invitrogen Molecular Probes (Eugene, OR, USA).

Synthesis of PEG–PBLA–PLys(Z) Triblock Copolymer

A triblock copolymer, PEG–PBLA–PLys(Z), was synthesized as previously described (20). Briefly, the PEG–poly (β-benzyl L-aspartate) diblock copolymer (PEG–PBLA) was synthesized by the ring-opening polymerization of BLA–NCA initiated by PEG–NH_2, followed by the additional ring-

opening polymerization of Lys(Z)-NCA to obtain PEG-PBLA-PLys(Z) (Fig. 1). Different solvents were used for the syntheses of PEG-PBLA with varying degree of polymerization (DP). For example, PEG-PBLA (DP of PBLA=14) was prepared as follows: BLA-NCA (25 eq to the terminal primary amino group of PEG-NH_2) in DMF was added to PEG-NH_2 in DMF under an argon atmosphere, and stirred at 35°C for 20 h. After confirming the end of the polymerization from the disappearance of specific peaks of NCA in the IR spectrum (IR Report-100 spectrometer (JASCO, Tokyo, Japan)), the solution was poured into a mixture of *n*-hexane and ethyl acetate (6:4) to precipitate PEG-PBLA, and the precipitate was filtered and dried *in vacuo*. A series of PEG-PBLA with longer PBLA segments was prepared by a similar protocol with necessary changes in reaction conditions, including molar feed ratios of PEG-NH_2 to BLA-NCA, solvents and reaction times, as summarized in Table I. The obtained PEG-PBLAs were subsequently used for the ring-opening polymerization of Lys(Z)-NCA. Lys(Z)-NCA (50 eq to terminal primary amino group of PEG-PBLA) in a mixture of DMF and dichloromethane was added to PEG-PBLA in dichloromethane (final molar ratio of DMF to dichloromethane=1:10) under an argon atmosphere, and stirred at 35°C for 40 h. After confirming the end of the polymerization as in the case of the polymerization of BLA-NCA, the solution was poured into the 6:4 mixture of *n*-hexane and ethyl acetate to precipitate PEG-PBLA-PLys (Z), and the precipitate was filtered and dried *in vacuo*. Then, acetylation of the amino group of the N-terminal of PEG-PBLA-PLys(Z) was performed using acetic anhydride (3 eq to the terminal amino group of PEG-PBLA-PLys(Z)) in dichloromethane solution.

For estimation of the DP and molecular weight distribution (Mw/Mn) of the obtained PEG-PBLA-PLys(Z), a gel permeation chromatography (GPC) measurement was carried out using a TOSOH HLC-8220 equipped with TSKgel columns (Super AW4000 and Super AW3000X2), and an internal refractive index (RI) detector. NMP with 50 mM LiBr was used as an eluent at a flow rate of 0.3 ml min^{-1} at 40°C.

Preparation of PEG-PAsp(DET)-PLys Triblock Copolymer

Introduction of 1,2-diaminoethane units into the side chain of the PBLA segment in PEG-PBLA-PLys(Z) was performed by aminolysis reaction with excess of DET molecules (13), followed by the deprotection of the Z group with HBr/AcOH (Fig. 1). The typical synthetic procedure of PEG-PAsp(DET)-PLys with DP of PAsp(DET)=36 and PLys=50 was as follows: Three hundred milligram of PEG-PBLA-PLys(Z) (9.2 μmol) was lyophilized from benzene

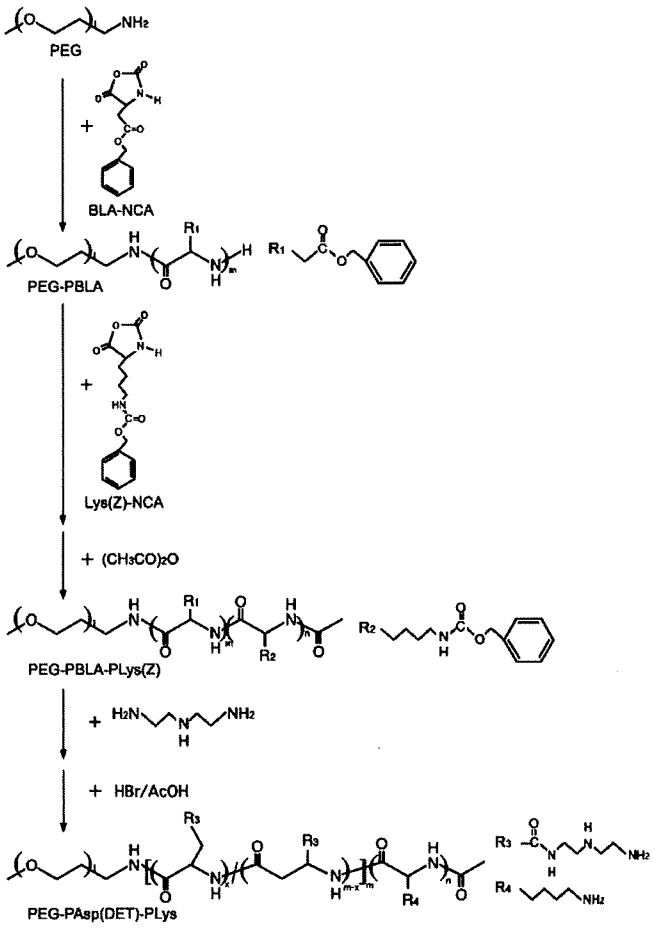

Fig. 1. Synthetic procedure of triblock copolymer, PEG-PAsp (DET)-PLys.

solution and dissolved into 6 mL of DMF. DET (1.8 mL, 16.7 mmol, 50 eq to benzyl groups of PBLA) was added under an argon atmosphere, and stirred at 40°C for 24 h. The mixture was dropped into diethyl ether (80 mL) with stirring, and then the white precipitate was filtered and redissolved in trifluoroacetic acid (2 mL). To deprotect the Z group, HBr (30% in acetic acid) was then added and stirred for 1 h, after which the solution was dropped into diethyl ether (40 mL) with stirring, and the resulting precipitate was purified by filtration and dried *in vacuo*. The crude product was dissolved in distilled water, dialyzed against 0.01 N HCl and then distilled water, and lyophilized to obtain the final product, PEG-PAsp(DET)-PLys as a hydrochloride salt form. The introduction of 1,2-diaminoethane units into the side chain of PAsp and the deprotection of Z group from the PLys(Z) segment were confirmed by ^1H NMR measurement (D_2O,

Table I. Reaction Condition and Composition of PEG-PBLA-PLys(Z)

Code	Molar feed ratio (PEG:BLA:Lys(Z))	Solvent/reaction time (h) for BLA polymerization	Solvent/reaction time (h) for Lys(Z) polymerization	DP of PBLA-PLys (Z)[a]	Mw/Mn[b]
PAsp14(DET)Lys48	1:25:50	DMF/20	DMF+CH_2Cl_2 (1:10)/40	14-48	1.16
PAsp36(DET)Lys50	1:45:50	DMSO/40	DMF+CH_2Cl_2 (1: 10)/40	36-50	1.13
PAsp66(DET)Lys47	1:80:50	DMF + CH_2Cl_2 (1:10)/40	DMF + CH_2Cl_2 (1:10)/40	66-47	1.28

[a] Determined from ^1H NMR.
[b] Determined from GPC.

80°C). In addition, other triblock copolymers, PEG-*b*-poly[*N*-(3-morpholylpropyl)aspartamide]-*b*-PLys (PEG–PAsp(APM)–PLys) and PEG-*b*-poly[*N*-(5-aminopentyl)aspartamide]-*b*-PLys (PEG–PAsp(DAP)–PLys), were similarly prepared by the aminolysis reaction of PEG–PBLA–PLys(Z) with 4-(3-aminopropyl)morpholine (20) and 1,5-diaminopentane (23), respectively. An ^{1}H NMR spectrum was measured with a JEOL EX300 spectrometer (JEOL, Tokyo, Japan). Chemical shifts are reported in ppm downfield from 3-(trimethylsilyl) propionic acid-d_4 sodium salt.

Cytotoxicity of PEG–PAsp(DET)–PLys Triblock Copolymer

A quantitative colorimetric assay with Cell Counting Kit-8 (Dojindo, Kumamoto, Japan) was carried out to evaluate cytotoxicity of block copolymers. This kit utilizes a colorimetric change from a soluble tetrazolium salt (WST-8) to WST-8 formazan by cytosolic dehydrogenases. Huh-7 cells (5,000 cells) were plated on 96-well plates and incubated overnight in 100 μL of DMEM containing 10% FBS. Then, the medium was changed to 100 μL of fresh medium containing 10% FBS and the polymers with various concentrations. After 24 h incubation, the medium was replaced with 100 μL of medium containing 10% FBS without polymers, followed by additional 24 h incubation. The medium was replaced with 120 μL of medium containing 10% FBS and 20 μL of Cell Counting Kit-8 solution, and then, incubated at 37°C for 3 h. The absorbance at 450 nm of the produced WST-8 formazan in each well was measured using a microplate reader (Model 680, Bio-rad). The cytotoxicity of block copolymers was estimated as a growth inhibitory concentration required for 50% reduction in cell population (IC50). The IC50 value of each block copolymer was calculated from a ratio of the obtained absorbance with the polymer to control without polymers. The results are presented as means and standard errors obtained from eight samples.

Preparation of PEG–PAsp(DET)–PLys/pDNA Polyplex Micelle

Each polymer was dissolved in 10 mM Tris–HCl (pH 7.4) buffer at a concentration of 2–5 mg/mL. These polymer solutions were then mixed with pDNA solution in 10 mM Tris–HCl (pH 7.4; final pDNA concentration: 33 μg/mL for *in vitro* assay and 100 μg/mL for *in vivo* assay) at varying mixing ratios.

Ethidium Bromide Exclusion Assay

Each polyplex micelle solution with 33 μg pDNA/mL, prepared by simply mixing pDNA and block copolymers at varying mixing ratios in 10 mM Tris–HCl (pH 7.4), was diluted to 10 μg pDNA/mL containing 2.5 μg EtBr/mL and 150 mM NaCl with the same buffer. The fluorescence intensity of the polyplex micelle solutions at λ=590 nm excited by UV laser (365 nm) was measured using a NanoDrop (ND-3300 Fluorospectrometer, Wilmington, DE, USA). The reference was set with 10 mM Tris–HCl (pH 7.4). The relative fluorescence intensity was calculated as follows:

$$F_r = (F_{\text{sample}} - F_0)/(F_{100} - F_0)$$

where F_{sample} is the fluorescence intensity of the micelle samples, F_{100} is that of the free pDNA, and F_0 is the background without pDNA. The results are presented as a mean and standard deviations (SD) obtained from three samples.

Dynamic Light Scattering and Zeta Potential Measurements

DLS and zeta potential measurements were performed using a Zetasizer nanoseries (Malvern Instruments Ltd., UK) at a detection angle of 173° and a temperature of 37°C. An He–Ne laser (λ=633 nm) was used as an incident beam. Polyplex solutions with various N^+/P ratios were prepared to a pDNA concentration of 33 μg/mL in 10 mM Tris–HCl (pH 7.4) buffer. The N^+/P ratio was defined as the molar ratio of protonated amino groups in block copolymers at pH 7.4 to phosphate groups in pDNA. The protonation degrees of lysine and Asp(DET) units at pH 7.4 were estimated to be 1.0 and 0.5, respectively, from the potentiometric titration results (13,24). In the DLS measurement, the sample solutions were injected into a small glass cuvette (volume: 12 μL), ZEN2112 (Malvern Instruments, Ltd.). The data obtained from the rate of decay in the photon correlation function were analyzed by the cumulant method, and the corresponding hydrodynamic diameter of the micelles was then calculated by the Stokes–Einstein equation (25). In the case of zeta potential measurement, the sample solutions were injected into folded capillary cells (Malvern Instruments, Ltd.). From the obtained electrophoretic mobility, the zeta potential was calculated by the Smoluchowski equation:

$$\zeta = 4\pi\eta\upsilon/\varepsilon$$

where η is the viscosity of the solvent, υ is the electrophoretic mobility, and ε is the dielectric constant of the solvent. The results are presented as a mean and SD obtained from three samples.

In Vitro Transfection (Luciferase Assay)

Huh-7 cells (20,000 cells) on 24-well culture plates were incubated with polyplex micelles containing 1 μg pDNA (Lys/Phosphate=2) in 400 μL of DMEM containing 10% FBS, followed by 24-h incubation and replacement with fresh medium. At 24 h post-incubation, the cells were washed with 400 μL of Dulbecco's PBS, and lysed with 200 μL of the cell culture lysis buffer (Promega). The luciferase activity of the lysates was evaluated from the photoluminescence intensity using the Luciferase Assay System and a Mithras LB 940 (Berthold Technologies). The obtained luciferase activity was normalized with the amount of proteins in the lysates determined by the Micro BCA™ Protein Assay Reagent Kit. The results are presented as means and standard errors obtained from four samples.

Cellular Uptake Study of Polyplex Micelles

pDNA was radioactively labeled with ^{32}P-dCTP using the Nick Translation System (Invitrogen, San Diego, CA, USA). Unincorporated nucleotides were removed using High Pure PCR Product Purification Kit (Roche Laboratories, Nutley, NJ, USA). After purification, 2 μg of labeled pDNA

was mixed with 400 μg of non-labeled pDNA. The polyplex micelle samples were prepared by mixing the radioactive pDNA solution with each polymer solution (Lys/Phosphate= 2 and 33 μg pDNA/mL). Huh-7 cells were seeded on 24-well culture plates in DMEM containing 10% FBS. After 24-h incubation, the cells were incubated for 24 h with 30 μL of the radioactive micelle solution (1 μg pDNA/well) in 400 μL of DMEM containing 10% FBS. The cells were then washed three times with Dulbecco's PBS and lysed with 400 μL of the cell culture lysis buffer. The lysates were mixed with 5 mL of scintillation cocktail, Ultima Gold (PerkinElmer, MA, USA), and the radioactivity of the mixtures was measured by a scintillation counter. The results are presented as means and standard errors obtained from four samples.

Intracellular Distribution of Cy5-labeled pDNA Evaluated Through Confocal Laser Scanning Microscope

pDNA was labeled with Cy5 using the Label IT Cy5 Labeling Kit according to the manufacturer's protocol. Huh-7 cells (50,000 cells) were seeded on a 35-mm glass base dish (Iwaki, Japan) and incubated overnight in 1 mL DMEM containing 10% FBS. After replacement of used medium with 1 mL of fresh medium, 90 μL of polyplex solution (Lys/Phosphate=2) containing 3 μg of Cy5-labeled pDNA was applied to the glass dish. After 24-h incubation, the medium was removed and the cells were washed three times with PBS. The intracellular distribution of each polyplex was observed by CLSM after staining acidic late endosomes and lysosomes with LysoTracker Green (Molecular Probes, Eugene, OR, USA) and nuclei with Hoechst 33342 (Dojindo Laboratories, Kumamoto, Japan). The CLSM observation was performed using LSM 510 (Carl Zeiss, Germany) with a ×63 objective lens (C-Apochromat, Carl Zeiss, Germany) at the excitation wavelengths of 488 nm (Ar laser), 633 nm (He–Ne laser), and 710 nm (MaiTai laser for 2-photon imaging) for LysoTracker Green (green), Cy5 (red), and Hoechst 33342 (blue), respectively.

In Vivo Enhanced Green Fluorescence Protein Expression in Subcutaneous Tumor Through Intravenous Injection of Polyplex Micelles

Human pancreatic adenocarcinoma cells (BxPC3) were grown in RPMI medium 1640 supplemented with 10% FBS. BALB/c nude mice (female, 5 weeks old) were obtained from Charles River Laboratories (Tokyo, Japan). All animal experimental protocols were performed in accordance with the Guide for the Care and Use of Laboratory Animals as stated by the NIH. BxPC3 cells (5×10^6 cells in 100 μL of PBS) were injected subcutaneously into the BALB/c nude mice and allowed to grow for 2–3 weeks to reach the proliferative phase. TβR-I inhibitor, dissolved to 5 mg/mL in DMSO and diluted by 100 μL of PBS, was intraperitoneally injected at 1 mg/kg 24 h before polyplex micelle administration. Polyplex micelles (Lys/Phosphate=2) containing EGFP gene in 200 μL of 10 mM HEPES buffer (pH 7.4) were intravenously injected through the tail vein at a dose of 20 μg pDNA/mouse. The mice were sacrificed 3 days after the injection. Tumors were excised, fixed with 10% formalin, and frozen in dry-iced acetone. The frozen samples were further sectioned at a 10-μm thickness in a cryostat. Immunostaining was carried out using anti-PECAM-1 antibody followed by Alexa647-conjugated secondary antibody for staining of vascular endothelial cells. The samples were observed by LSM 510 at excitation wavelengths of 488 and 633 nm for EGFP (green) and Alexa647 (red), respectively.

RESULTS

Preparation of PEG–PAsp(DET)–PLys Triblock Copolymer

A triblock copolymer of PEG, PBLA, and PLys(Z) (PEG–PBLA–PLys(Z)) as a precursor of the cationic triblock copolymer, PEG–PAsp(DET)–PLys, was synthesized by the two-step ring-opening polymerization of BLA–NCA (step 1) and Lys(Z)–NCA (step 2), initiated from the primary amine of PEG–NH_2 as shown in Fig. 1. In this way, a series of triblock copolymers with varying DPs of PBLA and PLys(Z) segments were prepared. As summarized in Table I, the obtained PEG–PBLA–PLys(Z)s were confirmed to have narrow Mw/Mn from the GPC, and the number of repeating units in PBLA and PLys(Z) segments was calculated from the peak intensity ratio of PBLA and PLys(Z) to PEG in the ^{1}H NMR spectra (data not shown). The conversion of flanking benzyl ester in the PBLA segment to *N*-(2-aminoethyl)-2-aminoethyl group was carried out by aminolysis reaction of PEG–PBLA–PLys(Z) with DET, followed by deprotection of the Z group of the PLys(Z) segment to obtain PEG–PAsp (DET)–PLys. The quantitative conversion of PBLA to PAsp (DET) and the complete deprotection of Z group were verified by ^{1}H NMR from the peak intensity ratio of the methylene protons in the *N*-(2-aminoethyl)-2-aminoethyl group ($H_2N(CH_2)_2NH(CH_2)_2NH$–, δ=3.1–3.5 ppm) to the β-methylene protons in the poly(aspartamide) (–$CHCH_2CO$–, δ=2.8 ppm) and the disappearance of the Z group peaks ($C_6H_5CH_2$–, δ=7.3 and 5 ppm), respectively, as typically seen in Fig. 2. The obtained PEG–PAsp(DET)–PLys was abbreviated as PAspX(DET)LysY, where X and Y represent the DP of the PAsp(DET) and PLys segments, respectively. Similarly, control diblock copolymers, PEG–PAsp(DET) and PEG–PLys, were abbreviated as PAspX(DET) and PLysY, respectively.

Cytotoxicity of PEG–PAsp(DET)–PLys Triblock Copolymer

The cytotoxicity of block copolymers, PEG–PAsp(DET), PEG–PLys, and PEG–PAsp(DET)–PLys, was compared and summarized as IC50 values in Table II. Obviously, PEG–PAsp(DET) showed much lower cytotoxicity than the others. The IC50 value of PAsp36(DET)Lys50 at the basis of polymer concentration (μM) was the similar level to that of PLys48, indicating that introduction of PAsp(DET) intermediate segment between PEG and PLys has negligible influence on the cytotoxicity of the block copolymer.

Formation of PEG–PAsp(DET)–PLys/pDNA Polyplex Micelles

Complex formation of pDNA with the triblock copolymer (PAsp36(DET)Lys50) was confirmed by EtBr exclusion assay. While EtBr molecules are known to emit strong fluorescence with their intercalation to DNA duplexes,

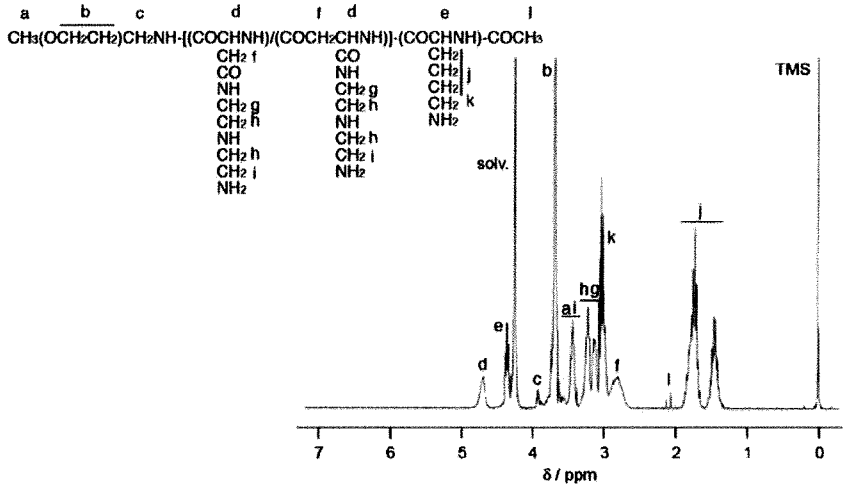

Fig. 2. ^{1}H NMR spectrum of the triblock copolymer, PAsp36(DET)Lys50. (Solvent, D_2O; temperature, 80°C; concentration, 10 mg/mL).

DNA condensation by cationic molecules inhibits such intercalation, resulting in decreased fluorescence. Accordingly, the measurement of the EtBr fluorescence allows the estimation of the process of pDNA condensation (26). The obtained fluorescence data are shown in Fig. 3a. The N/P ratio was defined as the residual molar ratio of total amino groups in the block copolymer to phosphate groups in the pDNA. The fluorescence change in PAsp36(DET)Lys50 seems to reach a plateau at an N/P ratio of 1.5. On the other hand, PLys48 and PAsp39(DET) as control diblock polycations reached plateaus at different N/P ratios; i.e., 1 for PLys48 and 2 for PAsp39(DET). In the plateau region, the fluorescence intensity was similar between PLys48 and PAsp36(DET)Lys50 possessing the PLys segment, while PAsp39(DET) showed higher fluorescence intensity than the others. This result suggests that the PLys segment may have higher ability of pDNA condensation than the PAsp(DET) segment to induce effective dye-exclusion. Then, the fluorescence data was replotted against the residual molar ratio of protonated amino groups to phosphate groups (N^+/P ratio; Fig. 3b). The protonation degree of Lys and Asp(DET) units at pH 7.4 was defined as 1.0 and 0.5, respectively, which were determined from potentiometric titration results of PEG–PLys (24) and PEG–PAsp(DET) diblock copolymers (13). Interestingly, in Fig. 3b, fluorescence profiles of all the samples showed similar trends, leveling off around the N^+/P ratio of 1, indicating that the protonated fraction of amino groups principally participates in the complexation with phosphate groups in the pDNA.

Table II. Growth Inhibitory Effects of the Block Copolymers Against Huh-7 Cells

Sample	IC50		
	Polymer concentration (μg/mL)	Polymer concentration (μM)	Amine concentration (μM)
PAsp68(DET)	>225	>7.35	>1,000
PLys48	26.1±1.4	1.2±0.1	57.0±3.1
PAsp36(DET)Lys50	29.5±0.8	0.9±0.04	114.4±4.9

Size and Zeta Potential of PEG–PAsp(DET)–PLys/pDNA Polyplex Micelles

The size and surface charge of gene vectors crucially affect their biological performance. Thus, these values of the polyplex micelles were determined by DLS and zeta potential measurements, respectively. As shown in Fig. 4a, the size of polyplex micelles gradually decreased with the N^+/P ratio, converging to the range of 60–80 nm in the region of $N^+/P>2$. The polyplex micelles from the triblock copolymer (PAsp36(DET)Lys50) were slightly smaller in size than those from the diblock copolymers (PAsp39(DET) and PLys48). As seen in Fig. 4b, all of the polyplex micelles showed almost neutral zeta potential at the N^+/P ratio of 1. Nevertheless, the micelles kept their initial size without any agglomeration even after overnight standing, as is consistent with the formation of a PEG palisade surrounding the polyplex core. Increasing the N^+/P ratio from 1 caused an increase in the zeta potential to a positive value, presumably due to the adsorption of excess block copolymers to the polyplex micelles as previously observed for PEG–P[Lys-*random*-Asp(DET)] block copolymer systems (19). The most prominent increase in the zeta potential with N^+/P was observed for the PAsp36(DET)PLys50 system, which may be explained by the decrease in PEG density of polyplex micelles due to the relative increase in the total length of cationic segments in the block copolymers; e.g., 39 for PAsp39(DET), 48 for PLys48, and 86 for PAsp36(DET)Lys50. Providing the micelles have the same compositional N^+/P ratio at a given feeding N^+/P ratio, the density of PEG should decrease with an increase in the length of the cationic segment. In this regard, the values of the zeta potential were compared between PAsp36(DET)Lys50 triblock micelles and PLys109 diblock (PEG–PLys) micelles having longer-length cationic PLys segments (Fig. 4c). Obviously, the PAsp36(DET)Lys50 micelles still had higher zeta potential than the PLys109 micelles. This finding indicates that the zeta potential of polyplex micelles in the region of excess block copolymers is not simply correlated to the length of the cationic segment, and that the difference in the chemical structure of cationic amino acid residues, in this case Lys and PAsp(DET), crucially affects the composition and structure of the polyplex micelles.